Friedrich-Alexander-Universität
Faculty of Sciences

Master's Thesis
in Physics

Sensitivity Studies for Galactic and Extragalactic Neutrino Fluxes with IceCube and KM3NeT/ARCA

Anke Katharina Mosbrugger

Supervisor: Prof. Dr. Claudio Kopper

Erlangen Centre for Astroparticle Physics (ECAP),
Friedrich-Alexander-Universität Erlangen-Nürnberg

Date of submission: December 16, 2025

Abstract

Accurate pointing and high detection efficiency when observing the Galactic Plane with muon neutrinos rely on precise muon track reconstruction. To suppress the dominant background of atmospheric muons, the Earth is used as a natural filter. This yields a pure neutrino dataset on the hemisphere below the local horizon. Therefore, combining data from neutrino telescopes in both hemispheres, IceCube in the Southern Hemisphere and KM3NeT in the Northern Hemisphere, increases sensitivity to an anisotropic astrophysical neutrino flux. For example, this is useful when observing the Galactic Plane. This thesis presents joint sensitivity studies obtained using MC datasets from the IceCube and ARCA detectors. Studies of the diffuse astrophysical neutrino flux are performed using a binned forward-folding likelihood approach. For IceCube, all statistical modeling is performed using the NNMFit framework. However, to encourage collaborative work and modernize the software, the open-source framework PyFF is being tested. This thesis presents the initial steps in implementing an ARCA21 diffuse all-sky analysis, including muon background and detector systematic handling, in this framework. The principle of using PyFF for ARCA analyses is evaluated by comparing it to other KM3NeT analyses.

Contents

1 Introduction

The first astronomical observations began several thousand years ago [1]. It started by observing the light of astronomical objects seen by eye. In the last century, by the development of telescopes, the observation of light from the universe in frequencies other than visible light began. With that, lower frequencies like radio-frequency or higher frequencies, for example, in the gamma-ray regime, can be observed. This made the discovery of new astronomical objects possible. Additionally, our understanding of these objects and the mechanisms of the universe improved. But not only are photons produced in astronomical objects. Instead, there exist more messenger particles than photons, such as astrophysical neutrinos. The astrophysical neutrinos were first discovered by the IceCube neutrino telescope in 2013 [2]. This opens the field of neutrino astronomy. Neutrinos are not deflected and are only rarely absorbed or scattered in dense environments. Making them an ideal messenger particle for understanding processes in the universe.

A recent discovery of the IceCube detector is the neutrino emission in the galactic plane with a significance of 4.5σ [3]. Still, the processes of neutrino production in our Galaxy are not fully understood yet. One problem is the low detection rate of astrophysical neutrinos compared to the atmospheric background. Statistically, within the IceCube detector, a ratio of 10^8 atmospheric background events to one astrophysical event is measured [3]. When focusing on neutrino events detected with high directional resolution (track events), the IceCube detector is only able to observe neutrinos from the Northern sky. The Southern sky region has to be cut off due to high backgrounds from that direction. As shown in Figure 1.1, the galactic center region is located in the Southern sky. So, it cannot be observed with track events in IceCube.

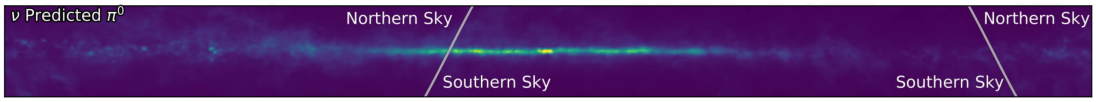

Figure 1.1: Neutrino flux predicted from gamma-ray observations for the galactic plane. The neutrino emission is shown in galactic coordinates. The galactic center is the brightest spot in the middle. It is located on the Southern Sky of the Earth [3].

However, further neutrino telescopes, which can observe the galactic center region with track events, are currently being built or will be built in the future. One that

is currently under construction is KM3NeT/ARCA, located in the Mediterranean Sea. The ARCA detector can, due to its location on Earth, observe about 90% of the galactic plane by track events as shown in Figure 1.2. As the detector is currently under construction, its detection volume and livetime are small compared to IceCube.

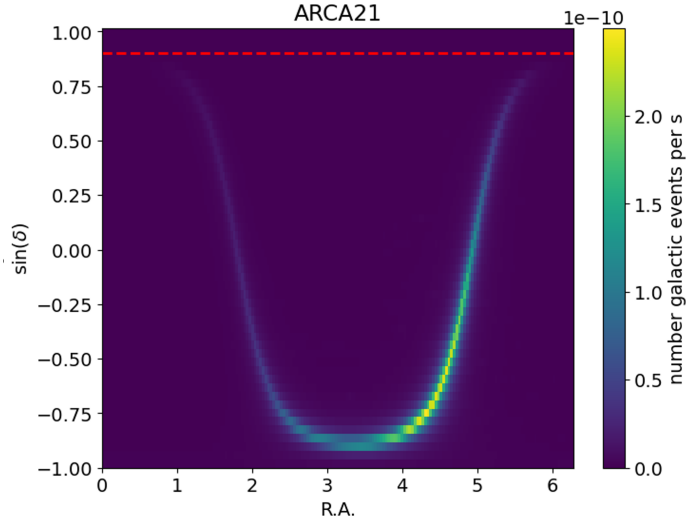

Figure 1.2: Expected neutrino flux from the galactic plane according to the CRINGE flux model for ARCA21. The plot shows the galactic plane in equatorial coordinates. The ARCA detector sees the galactic plane in the declination region $-1 < \sin(\delta) < 0.9$ with track events (below red dashed line). The galactic centre is located in the brightest region.

The sensitivity on the galactic plane with track events can be enhanced by combining the data of both the IceCube and ARCA detectors. With a joint analysis, the full galactic plane can be observed, and the limitations due to the low number of galactic neutrino events can be improved.

The objective of this thesis is to perform sensitivity studies on the joint ARCA-IceCube analysis of the galactic plane. To achieve this, NNMFit, the IceCube software used for diffuse analyses, is employed, and the ARCA Monte Carlo data are implemented. This thesis analyses the current detector status with ARCA21 and the future ARCA115 detector. As the NNMFit software is not currently publicly available, a new framework called PyFF is tested. PyFF is an open-source software framework for diffuse neutrino analyses. This thesis performs a diffuse all-sky analysis on simulated data for the ARCA21 detector. The aim is to validate the functionality of PyFF and test the ARCA21 implementations of background fluxes and detector systematics, modernizing the current ARCA all-sky measurement. In the end, the Asimov test results are compared to current KM3NeT diffuse all-sky analyses.

2 High-Energy Neutrino Physics

In order to analyse the astrophysical or galactic neutrino flux, it is necessary to understand the fundamentals of neutrino astronomy. This chapter provides an introduction to the fundamentals of neutrino physics and explains the motivation behind neutrino astronomy. It also describes how high-energy neutrinos can be detected.

2.1 Neutrinos

The neutrino as a particle was first postulated by Wolfgang Pauli in 1930 [4]. The newly postulated particle solved the contradiction of a continuous energy spectrum in the β-decay when only assuming electrons emitted in this decay. Three years later, Enrico Fermi was able to include the neutrino in his theory of the β-decay, describing it as a massless and chargeless particle. The first neutrino discovered by an experiment was the electron antineutrino in the reactor experiment conducted by Clyde L. Cowan and Frederick Reines, published in 1956. This was followed by the discovery of the muon and tau neutrinos in later decades.

Nowadays, we can classify the neutrino within the Standard Model of particle physics as a fermion, as it has a spin of 1/2 [5]. More precisely, the neutrino belongs to the class of leptons (in contrast to the quarks) which can be subdivided into three generations (referred to as flavors), ν_e, ν_μ, and ν_τ, each having an electrically charged partner particle, together referred to a "weak iso-doublets": e^-, μ^-, τ^-.

In contrast to their doublet partners, neutrinos do not interact via the electromagnetic interaction. Furthermore, as leptons, they do not interact via the strong interaction. Thus, in addition to gravity, neutrinos interact only via the weak interaction. Neutrinos are referred to as almost massless. However, since the discovery of neutrino oscillation, it is known that different mass eigenstates of a neutrino exist. The current upper limit for the neutrino mass, as set by the KATRIN experiment, is $m_\nu < 0.45\,\mathrm{eV}$ [6].

Neutrinos interact with matter only via the weak interaction (by exchanging either a $W^\pm$- or a Z^0-Boson) [7]. Their cross-section for the interaction with matter is very low compared to charged or more massive particles. As they are rarely absorbed by matter and are not deflected by magnetic fields, they are ideal messengers for observing astronomical objects. By detecting and reconstructing a neutrino's path,

one knows the direction of its origin. That opened the field of neutrino astronomy and the development of neutrino telescopes (discussed in section 2.4). Using these telescopes, neutrinos from various sources are detected (see section 2.3). In general, within this thesis, only high-energetic neutrinos ($> 100\,\mathrm{GeV}$) are discussed.

2.2 Cosmic Rays

Cosmic rays (CR) are a non-thermal population of particles originating from extraterrestrial sources [8]. They consist mostly of protons and atomic nuclei. They have a characteristic energy spectrum reaching from tens of MeV to the EeV energy range. Cosmic rays are accelerated to very high energies, but the mechanisms for producing and accelerating such particles are not yet fully understood. The characteristic energy spectrum follows a falling power-law $\frac{\mathrm{d}N^{\mathrm{CR}}}{\mathrm{d}E} \propto E^{-\gamma^{\mathrm{CR}}}$ (seen in Figure 2.1) [8]. Only the spectral index γ^{CR} changes at characteristic energies, giving hints to their origin. Cosmic ray particles between hundreds of MeV and a few PeV are believed to originate from galactic sources. Candidates are supernova remnants, star cluster winds, or, among others, the Galactic Center region, which could accelerate the particles. Above the EeV energy range, Cosmic rays are most likely from extragalactic sources. They are possibly accelerated by active galactic nuclei, gamma-ray bursts, or starburst galaxies.

The fundamental question when observing particles with such high energies is about the acceleration mechanisms in these astronomical objects. The standard explanation is currently the Fermi acceleration [10]. That mechanism is based on the creation of a shock wave of magnetized plasma in astronomical objects. Charged particles gain energy by repeatedly crossing that shock front. This acceleration mechanism is not specific to an astrophysical object. The change in the spectral index for different sources can be explained by a slowdown of the shock wave by the accelerated particles, or by the influence of the Milky Way on the observed cosmic rays at Earth. However, only a fraction of the charged particles can leave the source region of a high-density environment with strong magnetic fields. Therefore, these particles, predominantly protons p, re-interact with the dense environment or the photon γ background. In this re-interaction process, neutral π^0 and charged pions $\pi^{\pm}$ are created. Additionally also other hadronic products, denoted by X, can be produced [5]:

$$p + \gamma \rightarrow \pi^{+} X + n \tag{2.1}$$

$$p + \gamma \rightarrow \pi^{0} X + p \tag{2.2}$$

or

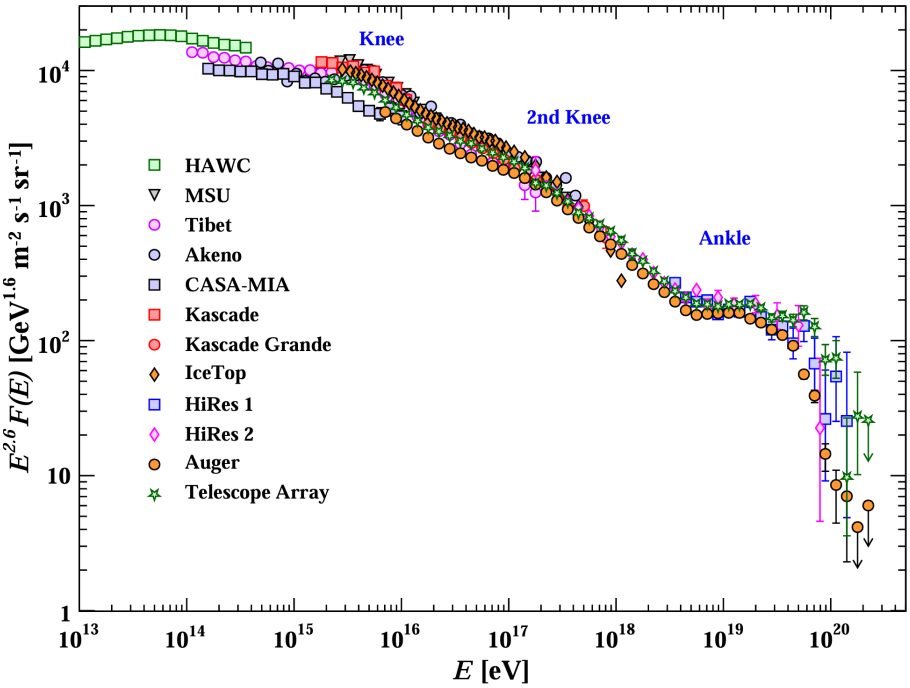

Figure 2.1: Characteristic energy spectrum of cosmic rays from different air shower experiments. The cosmic ray flux is multiplied by $E^{2.6}$ and shown as a function of Energy. The flux follows approximately a broken power-law, where the spectral index γ^{CR} changes at specific energies, denoted as the Knee, the 2nd Knee, and the Ankle. Figure taken from [9].

$$p + p \rightarrow \pi^0 + X \tag{2.3}$$

$$p + p \rightarrow \pi^{\pm} + X \tag{2.4}$$

The charged pions decay into muons and neutrinos $\pi^{\pm} \rightarrow \mu^{\pm} + \overset{(-)}{\nu}_{\mu}$, whereas the muons also decay to an electron and neutrinos $\mu^{\pm} \rightarrow e^{\pm} + \overset{(-)}{\nu}_{e} + \overset{(-)}{\nu}_{\mu}$. The neutrinos, in contrast to the charged particles, do not re-interact in the dense environment and can escape. Therefore, the neutrino flux from astronomical objects is directly related to the acceleration mechanism of the cosmic rays.

That is why neutrinos can help answer the question of particle acceleration mechanisms in the universe. As they also cannot be deflected, neutrinos detected at Earth directly point back to their source of origin.

2.3 Neutrino Fluxes

The discovery of an astrophysical neutrino flux in 2013 by the IceCube Collaboration opened the field of neutrino astronomy [2]. To perform such analyses on neutrinos from cosmic sources, the understanding of the processes in which neutrinos can be created and reach the detector becomes important. There are also a lot of background events, like atmospheric neutrinos and atmospheric muons, which need to be considered and understood.

2.3.1 Atmospheric and Prompt Flux

High-energy cosmic rays hitting molecules in Earth's atmosphere create a cascade of secondary particles evolving in the atmosphere. In a hadronic interaction, pions $\pi^{\pm}$ and kaons $K^{\pm}$ are produced. These mesons can decay into atmospheric muons and atmospheric neutrinos [5]:

$$\pi^{\pm} \to \mu^{\pm} + \overset{(-)}{\nu}_{\mu} \tag{2.5}$$

$$K^{\pm} \to \mu^{\pm} + \overset{(-)}{\nu}_{\mu} \tag{2.6}$$

The muons created decay into an electron and neutrinos as described in section 2.2, giving the conventional component of the atmospheric neutrino flux. The meson decay is dominant for lower energies, $E_{\nu} \ll 100\,\mathrm{GeV}$, and the neutrino energy spectrum follows the primary cosmic-ray spectrum. For higher energies, the re-interaction of Pions and Kaons becomes more important, and fewer neutrinos are produced. The energy spectrum becomes about one power steeper than the cosmic-ray spectrum [5]. The atmospheric neutrino spectrum is also dependent on the zenith angle at which the neutrinos reach the detector. With decreasing zenith angle, less dense air is crossed by the mesons. This makes re-interactions of Pions and Kaons less likely, and more neutrinos are produced by the Meson decay [11].

A subdominant component of the atmospheric neutrino flux is the prompt flux [12]. Higher-energy cosmic rays interact in the atmosphere, and heavier hadrons consisting of charm or bottom quarks can be produced. These heavy mesons decay promptly due to their high mass, among other particles, into neutrinos. Because of the prompt decay, no re-interaction of these mesons is possible. This results in the prompt component having no angular dependence, and following the cosmic-ray energy spectrum. Due to the harder energy spectrum, it becomes important for energies above $\sim 10\,\mathrm{TeV}$ [11]. Until now, a prompt neutrino flux had not been observed [12].

2.3.2 Diffuse Cosmic Flux

In contrast to measuring a single astrophysical neutrino source, the overall diffuse astrophysical flux is also studied in its energy spectrum and flux strength. The diffuse astrophysical flux does not resolve any specific sources in the angular distribution. The production mechanisms leading to that flux are not fully understood yet. There are various candidates for producing astrophysical neutrinos, e.g., choked Gamma-Ray-Bursts (GRBs), active galactic nuclei (AGNs), or tidal disruption events (TDEs) [13]. The acceleration mechanism of neutrinos from such sources is explained in section 2.2, as neutrinos are produced by cosmic rays that are accelerated in magnetic fields and interact in these dense environments. Consequently, the neutrino flux would follow the same power law as the initial cosmic rays originating from these astronomical sources.

2.3.3 Diffuse Galactic Flux

Cosmic rays can also interact within the denser environment of galaxies. In that process, neutral pions (cf. Equation 2.3) and charged pions (cf. Equation 2.4) are created. Neutral pions decay into photons $\pi^0 \rightarrow \gamma + \gamma$, whereas charged pions produce neutrinos in their decay [3]. The observation of the Milky Way in gamma rays is proven. It is the most prominent feature in the gamma observation above 1 GeV. The charged pions decay as described in section 2.2 into neutrinos. Therefore, knowledge of a gamma-ray flux also allows for the prediction of a diffuse neutrino flux from the Milky Way.

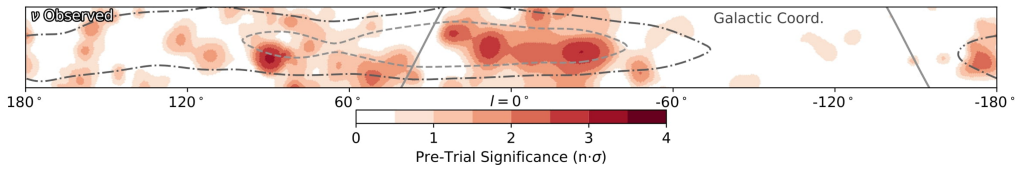

Figure 2.2: Significance for a neutrino flux from the galactic plane over the isotropic background flux. It is shown for the galactic band observed by the IceCube detector, leading to the discovery of a diffuse galactic neutrino flux with a significance of 4.5σ, taken from [3].

A diffuse galactic neutrino flux was discovered in 2023 by the IceCube Collaboration with a significance of 4.5σ (shown in Figure 2.2) [3]. However, various gamma-ray point sources in the Milky Way are also potential cosmic-ray accelerators and therefore can potentially emit neutrinos. An individual neutrino point source within the Milky Way could not be identified yet.

2.3.4 Atmospheric Muon Background

One main background in the high-energy neutrino detection are cosmic-ray induced muons. As explained in subsection 2.3.1, they are created by cosmic rays hitting the atmosphere. Muons have a mean lifetime of a few μs, which is long in comparison to the mesons produced. With enough energy, they can cross several kilometers of matter such as water and ice. To reach the IceCube detector at a depth $\sim 2\,\mathrm{km}$ they need a minimal energy of $\sim 0.5\,\mathrm{TeV}$ [5]. As mentioned in subsection 2.4.3, the neutrino signal and atmospheric muon signal are distinguished by using only up-going events. However, there are still mis-reconstructions of the event, and the classification of up-going events does not always work correctly. That is why it is important to also consider atmospheric muon contamination in the neutrino flux.

2.4 Neutrino Telescopes

The previous sections explain why the high-energy neutrino flux is interesting to investigate. This section describes how these neutrinos can be detected.

The detection mechanism of neutrino telescopes is based on detecting charged secondary particles, created from the weak interaction of neutrinos with a nucleon of the detector medium (see subsection 2.4.3). That means the neutrino itself cannot be observed, only products from its interaction with matter. The charged secondaries can then be detected via the Cherenkov effect [14]. This effect occurs in dielectric media with a refractive index $n > 1$ for charged particles traveling with a velocity v larger than the phase velocity of light $v > \frac{c}{n}$ in that medium. Some of the particle's energy is converted into light, resulting in a cone-shaped wave front traveling with the charged particle.

The low cross-section of neutrinos is a major challenge in detecting these particles. As an example, assuming a neutrino flux for a bright point-source similar to the Crab Nebula at energies in the TeV regime, the neutrino cross section is approximately $10^{-35}\,\mathrm{cm}^2$. Using one km^3 of water as a target volume, a rate of approximately 10 neutrinos per year is expected to interact within this volume [5]. Therefore, for the detection of high-energy neutrinos, large detector volumes are needed.

Gigatons of a transparent but dense medium for the detection of the Cherenkov light exist naturally on Earth in the form of water and ice. That is why the first km^3-scaled neutrino telescope, IceCube, was built in the Antarctic ice at the South Pole [5]. Another km^3-scaled neutrino telescope in the water of the Mediterranean Sea is currently under construction - ARCA by the KM3NeT collaboration.

2.4.1 IceCube

The IceCube neutrino telescope is located at the geographical South Pole. To reach the instrumented volume of $1\,\mathrm{km}^3$, 86 detector lines, each having 60 digital optical modules (DOMs), are frozen into the ice [5]. The DOMs, not in the DeepCore area, on one line have a spacing of 17 m, sitting in a depth between 1450 m and 2450 m (see Figure 2.3). The detector lines have a spacing of 125 m. The DeepCore area consists of six denser deployed detector lines and seven normal lines. It is optimized to detect lower-energy neutrinos. On the surface of the detector lines, the IceTop array is built. This consists of a pair of tanks near each line top, having two DOMs each. The IceTop array detects cosmic rays reaching the top of the detector. IceTop is used for investigating the cosmic ray flux, and it can be used for vetoing background events.

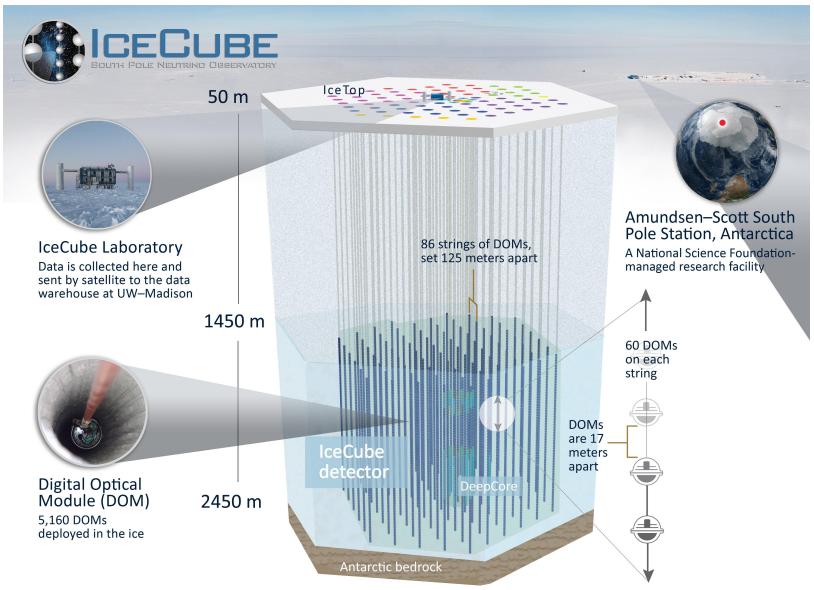

Figure 2.3: The IceCube neutrino telescope built in the Antarctic ice at the South Pole. The image shows the layout of the detector array consisting of 86 detector lines, each equipped with 60 DOMs, and was taken from the IceCube Collaboration [15].

Each of the 5,160 in-ice DOMs is equipped with one photomultiplier tube (PMT) and associated electronics. The PMT is sitting on the bottom half of the hemisphere, facing toward the Earth. They are specifically designed to detect the Cherenkov light of charged particles traveling through the ice, emitting light at a wavelength between 300 nm and 500 nm [16].

2.4.2 KM3NeT/ARCA

The KM3NeT collaboration is currently constructing two neutrino detectors in the seawater of the Mediterranean Sea, currently under construction: ARCA (Astroparticle Research with Cosmics in the Abyss) and ORCA (Oscillation Research with Cosmics in the Abyss). Both detectors contain mostly the same hardware, where the optical modules are aligned on vertical detector lines. In the ORCA detector, the detector lines are deployed much densely than in the ARCA detector [17]. Additionally, the DOMs on one line have a denser spacing in the ORCA detector. The reason for that is that each detector is optimized for its science case: ARCA detecting high-energy cosmic neutrinos and ORCA registering lower-energy atmospheric neutrinos. As this thesis focuses on high-energy neutrinos, only the ARCA detector is considered in the following.

The ARCA detector is located 100 km offshore from the town of Portopali di Capo Passero on Sicily. The detector lines, also called detection units (DUs), are anchored at a depth of 3500 m. They are each equipped with 18 DOMs with a spacing of 40 m [18]. The horizontal spacing of the DUs is about 100 m for ARCA. In comparison to IceCube, the DOMs contains more than one PMT. Instead, they have 31 PMTs each. The PMTs are arranged to detect light from all directions, where 19 PMTs sit on the lower hemisphere of the DOM. The PMTs are optimized to detect light in the same wavelength regime as the IceCube PMTs, as water and ice have about the same diffractive index [16].

The first building phase of the ARCA detector is planned to install one block of the ARCA detector, consisting of 115 DUs. The construction phase of KM3NeT 2.0 is planned to end with two building blocks of ARCA, consisting of 230 DUs [18]. With the two building blocks, ARCA will have an instrumented volume of about one cubic kilometer. The array design is shown in Figure 2.4. As of writing this thesis, 51 DUs are deployed and operational. During the construction, the deployed part of ARCA can already measure data. This raises the opportunity for first analyses, which can be performed with a smaller detector volume than the planned one. These analyses refer to a certain building phase by labeling the detector name ARCA with the number of DUs in operation during that time period. The most relevant ARCA configuration for this thesis is ARCA21, which is the ARCA detector with 21 DUs. The data obtained from that detector configuration has a livetime of 287 days.

2.4.3 Event Signatures in Neutrino Telescopes

The predominant interaction between high-energy ($E_\nu > 100\,\mathrm{MeV}$) neutrinos and nucleons of the detector material is deep-inelastic scattering. Consequently, two primary event signatures are observed in the detector: cascades and tracks (cf. Figure 2.5).

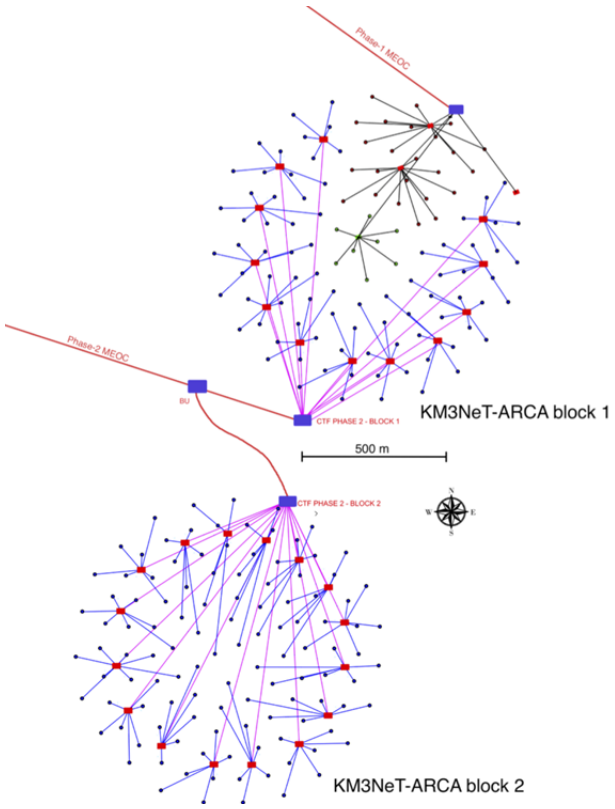

Figure 2.4: The ARCA detector is located 100 km offshore from the coast of Sicily in the Mediterranean Sea. After building phase 2.0, it is planned to consist of two building blocks, including 230 DUs. The image shows the top view of the layout, where blue and black dots indicate DUs of the planned cubic kilometer-sized detector array. The lines represent the different sea cables deployed in the Sea. The image is taken from [17].

The production of track-like events is exclusively attributable to muon neutrinos interacting via charged-current (CC) interaction with a nucleon N, exchanging a W^--Boson [5]:

$$\nu_\mu + N \rightarrow \mu^- + X \tag{2.7}$$

$$\overline{\nu}_\mu + N \rightarrow \mu^+ + X \tag{2.8}$$

In addition to the hadronic component X, a muon μ is created. The hadronic particles created additionally can directly re-interact with the surrounding medium and therefore produce a cascade of particles. High-energy muons can travel several kilometers through ice or water. As they travel through the detector medium, they lose energy and emit Cherenkov light. This is observed as a track signal in the detector

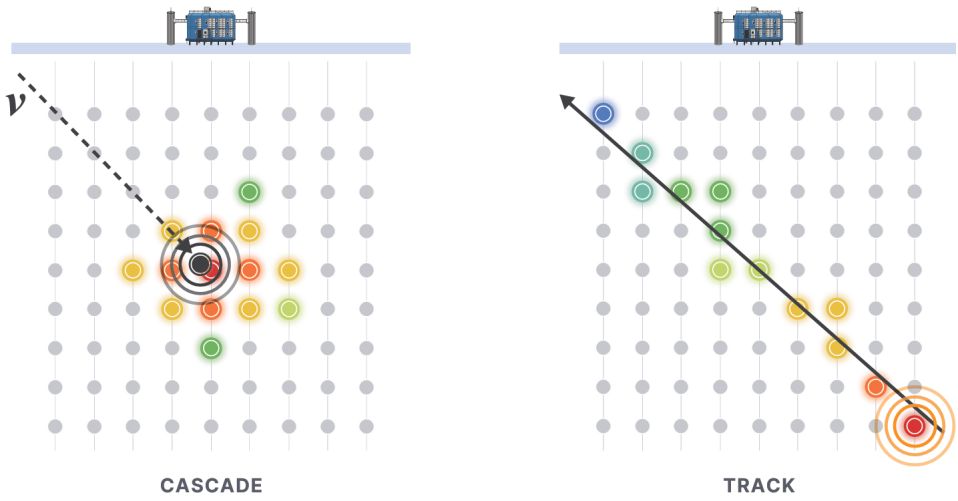

Figure 2.5: These sketches show the IceCube detector, detecting different event signatures. On the left is a neutrino interacting within the instrumented volume and creating a cascade signature. On the right is a muon from a neutrino interaction in the ice crossing the detector, which is seen as a track signature. All DOMs measuring a signal from the event are shown in color. The colors represent the arrival time of the light in the PMTs: red DOMs measure the signal earliest, followed by green, and then blue. Sketch taken from [19].

as shown in Figure 2.5 on the right. Only the energy deposited by a muon passing through the detector can be measured. Therefore, the neutrino energy is determined on a statistical basis. Since muons can travel several kilometers through ice, the CC interaction can occur either inside the detector, which is denoted as a starting track event, or outside the instrumented detector volume. There, the neutrino interacts with the surrounding medium, and only the muon passes through the detector as a throughgoing track event. For that, the concept of an effective area becomes important. It describes the hypothetical detector area that is able to detect every neutrino passing through this area. The effective area is energy and directionally dependent. In the case of track events, the effective area of a neutrino telescope can exceed the instrumented volume because high-energy neutrinos can interact outside of this volume and still be detected.

Cascade events can originate from a CC interaction between a nucleon and an electron neutrino

$$\nu_e + N \rightarrow e^- + X \tag{2.9}$$

$$\overline{\nu}_e + N \rightarrow e^+ + X \tag{2.10}$$

In this case, an electron and a hadronic shower are produced. These particles interact directly around the interaction point due to their small interaction length. The electron produces an electromagnetic cascade that carries most of the neutrino's energy, and the hadronic cascade carries $\sim 20\%$ of the remaining neutrino energy [5]. So the full neutrino energy is deposited in the detector. Alternatively, the cascade event can result from a neutral-current (NC) interaction involving a nucleon and a neutrino of any flavor ν_l:

$$\nu_l + N \rightarrow \nu_l + X \tag{2.11}$$

This results from a Z^0 boson-mediated interaction, whereby a neutrino leaves the interaction vertex with reduced energy and a hadron shower. Most of the energy is carried by the scattered neutrino, and only the hadronic cascade, which has about 30% of the energy, can be detected [20].

Both event types come with advantages and disadvantages for physical analyses. Cascade events generally have good energy resolution, because most of the light is emitted inside the detector. However, their spatial resolution is limited as they are typically several meters long ($\sim 10\,\mathrm{m}$) [5]. So their size is smaller than the spacing of optical modules in high-energy neutrino telescopes. Therefore, the energy resolution is worse for track events, but the spatial resolution of a neutrino-induced muon is less than one degree. At high energies, the directions of the neutrino and muon are approximately the same. Thus, by reconstructing the muon track, the spatial location of the neutrino's origin can be determined within the detector resolution of the muon direction.

In order to have an event sample with good spatial resolution, some analyses consider only track events. The main challenge is distinguishing signal events from muons resulting from the interaction of muon neutrinos and high-energy atmospheric muons reaching the detector. This is why the direction of a track passing through the detector is also important. Neutrino telescopes are located several kilometers deep in the sea or ice to shield them from lower-energy atmospheric muons. However, high-energy atmospheric muons can pass through several kilometers of the detector medium and might be detected. The Earth can be used as a shield that high-energy atmospheric muons can not pass through anymore. Therefore, upgoing muons with a zenith angle $z > 85°$ must result from neutrinos that have crossed the Earth [21].

3 Analysis Method

Two analyses were performed within this thesis. The first is a diffuse galactic analysis using the software framework NNMFit (NewNuMuFit) [22], and the second is a diffuse all-sky analysis using the software framework pyFF (pyForwardFolding) [23]. Both analyses are based on a forward-folding likelihood fit (cf. subsection 3.3.2). To perform such a fit, flux models that model the physical neutrino flux (described in section 2.3) must be implemented. Additionally, the weighted Monte Carlo events must be correctly implemented, including an event selection, as discussed in the following section. The following subsections will also discuss a method for muon background handling and the treatment of systematic uncertainties.

3.1 Flux Models

Each neutrino flux component (from section 2.3) considered in the analysis needs to be described by a physical model. The all-sky diffuse analysis considers the astrophysical flux as the signal and the atmospheric flux as the background. In the diffuse galactic analysis, all fluxes from the all-sky analysis are background, and the galactic neutrino flux is the signal.

The atmospheric flux is modeled by the Matrix Cascade Equation (MCEq) code [24]. It models the conventional and prompt neutrino flux by solving cascade equations for particle cascades in the atmosphere. With MCEq, splines are built containing a primary cosmic ray flux model and a hadronic interaction model. There are two splines built, one ($w_{\text{Gaisser-H4a}}$) with the cosmic ray model Gaisser-H4a and the interaction model Sibyll2.3c. The other one (w_{GSF}) uses the same interaction model, but the GSF model for the primary cosmic ray flux. Within the analysis, it is interpolated between those two model predictions by fitting an interpolation factor λ_{int}:

$$\lambda_{\text{int}} w_{\text{Gaisser-H4a}} + (1 - \lambda_{\text{int}}) w_{\text{GSF}} \tag{3.1}$$

Within this thesis, this factor is in all Asimov tests set to $\lambda_{\text{int}} = 1$. In addition to the flux models, a factor $\left(\frac{E_\nu}{E_{\text{median}}}\right)^{\Gamma}$ is implemented, accounting for uncertainties in the cosmic ray energy spectrum. The spectral index of this factor is fitted in the analysis. For all Asimov tests, the atmospheric spectral index is set to $\Gamma = 0$. The whole model

can then be scaled in the analysis by a flux normalization Φ_{conv} for the conventional atmospheric and Φ_{prompt} for the prompt flux.

The energy spectrum of the diffuse astrophysical neutrino flux is described by a single-power-law (SPL) spectrum for primary neutrino energy E_ν:

$$\Phi_{\text{astro}}(E_\nu) = \Phi_0^{\text{astro}} \times \left(\frac{E_\nu}{E_{\text{ref}}}\right)^{-\gamma_{\text{astro}}} \tag{3.2}$$

A reference energy E_{ref} is defined, so that the unit of the flux normalization is not spectral index dependent. Within this thesis, a reference energy of $E_{\text{ref}} = 100\,\text{TeV}$ is used. The free fit parameters in that flux are the flux normalization Φ_0^{astro}, with units $10^{-18}\,\text{GeV}^{-1}\,\text{cm}^{-2}\,\text{s}^{-1}\,\text{sr}^{-1}$, and the spectral index γ_{astro}.

For modeling the diffuse galactic neutrino flux, the CRINGE (Cosmic Ray-fitted Intensities of Galactic Emission) model is used [25]. This model predicts a diffuse galactic neutrino and gamma-ray flux, fitted to measured cosmic ray data.

The distribution of the diffuse galactic neutrino flux predicted with the CRINGE model is shown in Figure 3.1 in galactic coordinates. The galactic centre is in the centre of the Mollweide view. The model predicts the highest neutrino flux from that region. In the analysis, it is implemented in equatorial coordinates, with one free normalization Φ_{galactic} parameter for scaling the neutrino flux of the model.

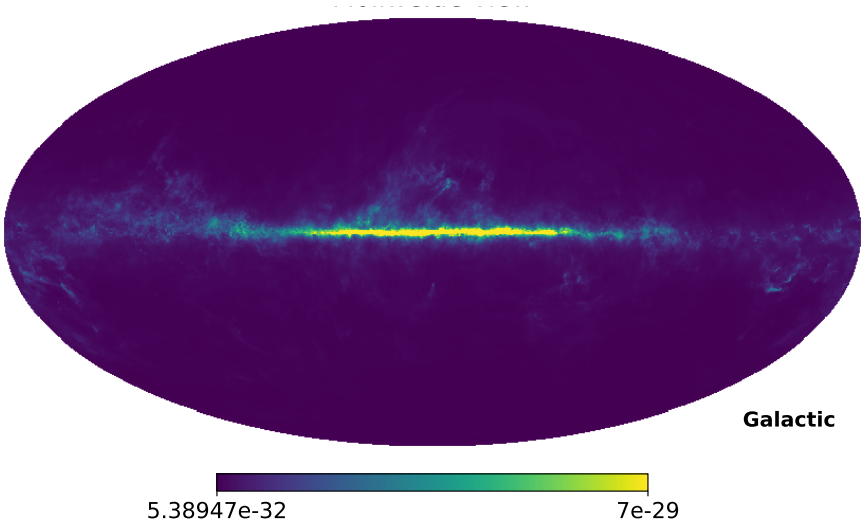

Figure 3.1: Mollweide view of the CRINGE model for the galactic neutrino emission in the galactic plane. The Plot shows the model in galactic coordinates; therefore, the galactic center is at the center of the Mollweide sky map with the highest neutrino flux.

3.2 Monte Carlo Simulations

Conclusions about the physical values of the incoming particle cannot be directly made by detecting a neutrino event without accounting for the detector response. To achieve this, a Monte Carlo (MC) simulation is used to model the expected events occurring in the detector from specific physical values. The MC simulation produces neutrino and atmospheric muon events, modelling their interaction in the detector. For an analysis, datasets are required to determine how these simulated events would be seen in the neutrino telescope. For that, a full chain is developed, processing the neutrino itself until the reconstructed simulations, which are then used for the analysis.

3.2.1 Event Weighting

The simulations for neutrino telescopes start by simulating the neutrino or atmospheric muon events. To account for a good statistical spectrum in the observation variables (usually true MC Energy E and direction via two angles ϕ, θ), the events are not simulated in a physical spectrum. Instead, a generation spectrum $f(E,\theta,\phi)^{\text{gen}}$ is used. To still be able to account for a physical spectrum, each event is simulated with a specific weight $w_{\text{evt}} = w_{\text{gen}} \cdot f(E,\theta,\phi)^{\text{phys}}$. Where $f(E,\theta,\phi)^{\text{phys}}$ is the physical spectrum and $w_{\text{gen}} = \frac{1}{f(E,\theta,\phi)^{\text{gen}}}$ the simulation weight with the simulated spectrum [26].

3.2.2 Simulated Dataset KM3NeT/ARCA

The KM3NeT/ARCA simulations start by simulating all-flavor high-energy neutrinos with the `gSeaGen` software package [27]. Each event is simulated with an $w_2 = \frac{n_{\text{tot}}}{f(E,\theta,\phi)^{gen}}$ weight, given in the units [GeVm^{2}sr] [28]. The atmospheric muon events are simulated by the MUPAGE software package, having a direct physical muon weight w_{muon}. Once the particle has been simulated, its propagation through the Earth and its interactions, as well as any possible secondary particles, are simulated.

In the next step, the light production and propagation through water, as well as the detection on the PMTs, is simulated. Additionally, background light from K40 decays, bioluminescence, and the PMT electronics are simulated.

In the end, the information about simulated hits on the PMTs has the same format as in the data, and the reconstruction algorithm used for the data can also be applied. For handling the track reconstruction, the JPP package [29] is used. So all events have the information of the true simulated properties and the reconstructed properties.

3.2.2.1 ARCA21 MC Simulations

The ARCA21 detector had a data-taking lifetime of 287.4 days. This lifetime is separated into multiple runs, each having a duration of a couple of hours. The simulation dataset (DST-format) for ARCA21 is taken from the mass procession of the KM3NeT collaboration with version v9.1. The DST (Data Summary Tape) files are summary files of the official KM3NeT MC production [30]. They include all simulated and reconstructed variables, but no direct PMT hit information to speed up analyses. This simulation is performed in a run-by-run approach. That means for each run during the data acquisition phase, a simulated dataset is created, containing atmospheric muons, all-flavor neutrinos, and pure noise simulations. For the simulations, the optical backgrounds retrieved from real data, as well as PMT response and efficiency, are used in each run [31].

Because of the run-by-run based approach, the weights per flux and detector lifetime are calculated by $w_{\text{flux, ARCA21}} = w_2 \cdot \Phi_{\text{flux}} / n_{\text{tot}} \cdot t_{\text{DAQ-livetime}}$, where w_2 is the generation weight in the simulation. n_{tot} is the total number of events simulated within the run, and $t_{\text{DAQ-lifetime}}$ is the time of one run.

3.2.2.2 ARCA115 MC Simulations

The ARCA115 detector is currently still under construction and therefore has no data-taking period yet. Within this thesis, the KM3NeT MC production for ARCA115 with version v6.0 is used. As this simulation at the moment can not be performed run-based, the flux weights are calculated by $w_{\text{flux, ARCA115}} = w_2 \cdot \Phi_{\text{flux}} / n_{\text{tot}}$ per second.

3.2.3 Simulated Dataset IceCube

In contrast to the ARCA simulation, IceCube does not use a run-by-run approach for simulating neutrino events. All flavor neutrino events are generated using the `NuGeN` [32] software and are randomly distributed within an injected spectrum of energy and direction. The propagation of the neutrinos through the Earth is modeled, as well as the interaction of neutrinos in the ice or bedrock near the detector. In the next step, the charged products (e.g., hadronic cascade or muons) of such an interaction are modeled, including their propagation through the ice. When modeling the Cherenkov photons, an ice model has to be considered. In the end, the DOM response is modeled, and the simulated hits are saved as the experimental data.

Within this thesis, the IceCube MC simulation set containing the Northern track selection (c.f. section 3.5.1.1) is used. The events contain some baseline weights w_{baseline} with a certain weight per second. The weights for each flux model i per second are calculated by multiplying by the flux $w_j = w_{\text{baseline}} \cdot \Phi_{\text{flux}}$. To account for a

detector lifetime, the weights have to be multiplied by the detector lifetime in seconds. Within this thesis a current detector lifetime for IceCube of 11.67 years is assumed.

3.3 Statistical Method

All analyses performed within this thesis use the forward-folding method. This is based on comparing the expected event distribution to the events observed in the detector by a likelihood function. For that, the observed events are binned in the reconstructed variables: (energy, zenith) for the diffuse all-sky analysis and (energy, declination, right ascension) for the galactic plane analysis. This gives a histogram containing the observed event numbers per bin. The expected event distribution is obtained by re-weighting MC simulated events. The weights depend on the flux parameters, free parameters in the description of the neutrino flux.

3.3.1 Analysis Histograms

Before performing the statistical analysis, the histograms containing the binned expectation are calculated. So for every bin j, the bin expectation is μ_j. This is constructed by summing up the event numbers per bin of each flux contribution. For example, for the diffuse flux, the bin expectation is given by

$$\mu_j(\boldsymbol{\theta}) = \mu_j^{\text{conv.}} + \mu_j^{\text{pompt.}} + \mu_j^{\text{astro.}} + \mu_j^{\text{muons.}} \tag{3.3}$$

It is dependent on the free flux parameters $\boldsymbol{\theta}$, as the bin expectation for each flux component is the sum over the flux weights w_i of the single events i:

$$\mu_j^{\text{flux}} = \sum_i w_i^j \tag{3.4}$$

The weight of a single event is then dependent on the simulated properties and the flux assumptions. Whereas the flux assumptions depend on the free fit parameters/flux parameters $\boldsymbol{\theta}$ within the flux models.

The data events are also binned in a histogram in the reconstructed variables. The number of data events per bin is denoted as d_j.

3.3.2 Forward-Folding Method

This method is referred to as forward folding, because the flux parameters are processed through the detector response before being compared to the data. Theoretical flux

models are defined in terms of true physical quantities and do not account for detector effects. To account for these effects, the Monte Carlo (MC) simulation provides true physical values at generation and corresponding reconstructed values after detector simulation and event reconstruction.

During the fitting process, the MC events are reweighted according to each trial set of flux parameters, using their true physical quantities. The weighted events are then binned according to their reconstructed quantities, whereby the detector response is implicitly incorporated.

The comparison between expected and detected events is performed in terms of a likelihood, comparing the binned number of expected events μ_j and the binned number of data events d_j over each bin j [33]:

$$\mathcal{L}(\mu_j(\boldsymbol{\theta})) = \prod_j \mathcal{L}^j_{\text{bin}}(\mu_j(\boldsymbol{\theta}); d_j) \tag{3.5}$$

This comparison in reconstructed space explicitly depends on the flux parameters through event reweighting, which ensures that the detector response is consistently incorporated into the model prediction throughout the fitting procedure.

In the following analyses, a Poisson likelihood and an effective likelihood (SAY likelihood) [34] are used for the fit.

3.3.3 Effective and Poisson Likelihood

When performing a binned likelihood analysis, the number of events is assumed to follow a Poissonian distribution. For one bin, the Poisson likelihood is given by [34]:

$$\mathcal{L}(\boldsymbol{\theta} \mid d) = \text{Poisson}(\mu(\boldsymbol{\theta}); d) = \frac{\mu(\boldsymbol{\theta})^d \, e^{-\mu(\boldsymbol{\theta})}}{d!} \tag{3.6}$$

The MC simulation is a statistical process and can only simulate a finite number of events. This can lead to statistical fluctuations in the number of MC events across the observable bins. This can result in statistical fluctuations in the number of MC events across the observable bins. Consequently, some bins may contain only a few MC events, resulting in significant statistical uncertainties in the MC-based expectation values. In the limit of large MC statistics, the uncertainty on the predicted expectation value becomes negligible. However, for limited MC statistics, some bins may contain only a small number of simulated events, leading to sizable uncertainties in the predicted expectation values.

The standard Poisson likelihood assumes that the expectation value in each bin is known exactly and accounts only for statistical fluctuations in the observed data. It

therefore neglects the additional uncertainty arising from finite MC statistics. This motivates the usage of the effective (SAY) likelihood. The SAY likelihood accounts for uncertainties in the MC based expectation values per bin $\sigma_j^2 = \sum_i (w_i^j)^2$, depending on the weights of the single MC events, and is given by [34]:

$$\mathcal{L}_{\text{eff}}(\boldsymbol{\theta} \mid d) = \left(\frac{\mu}{\sigma^2}\right)^{\frac{\mu^2}{\sigma^2}+1} \Gamma\left(d + \frac{\mu^2}{\sigma^2} + 1\right) \left[d!\, \Gamma\left(\frac{\mu^2}{\sigma^2} + 1\right) \left(1 + \frac{\mu}{\sigma^2}\right)^{d+\frac{\mu^2}{\sigma^2}+1} \right]^{-1} \tag{3.7}$$

In this likelihood function

where Γ is the gamma function, and μ and σ^2 depend on the model parameters $\boldsymbol{\theta}$ via the weight w_i^j. In cases where the number of MC events per bin increases, the SAY likelihood converges to the Poisson likelihood. Within this analysis, the SAY likelihood is used for testing the MC statistics. For example, for varying the number of bins or adding a binning axis.

3.3.4 Maximum Likelihood Method

When comparing the expected event distribution by the detected events, within the forward-folding workflow, the free flux parameters are fitted. The best-fit values are determined by minimizing the negative log-likelihood $-\log(\mathcal{L}(\mu_j(\boldsymbol{\theta})))$ for the flux parameters.

Additionally, the confidence intervals of the best-fit parameters are determined. This is done by varying a set of fit parameters $\boldsymbol{\alpha}$ on a fixed grid and minimizing the log-likelihood for the other free fit parameters [35]. This is referred to as a profile likelihood scan. Usually, it is done in one or two dimensions, so $\boldsymbol{\alpha}$ consists of one or two fit parameters. The ratio of the likelihood with all fit parameters free $\mathcal{L}(\boldsymbol{\theta} \mid d)$ and with some fit parameters fixed $\boldsymbol{\alpha}$, $\mathcal{L}(\boldsymbol{\theta}, \boldsymbol{\alpha} \mid d)$ is defined as the test-statistic [36]:

$$\text{TS} = -2 \cdot \log\left(\frac{\mathcal{L}(\boldsymbol{\theta}, \boldsymbol{\alpha} \mid d)}{\mathcal{L}(\boldsymbol{\theta} \mid d)}\right) = -2 \cdot \Delta\log(\mathcal{L}) \tag{3.8}$$

According to Wilk's Theorem [37], the test statistic follows a χ^2 distribution with n degrees of freedom, where n is the number of varied fit parameters in the profile likelihood. The test statistic can be translated into a p-value, giving an n-dimensional confidence interval $[\boldsymbol{a}, \boldsymbol{b}]$ (for $n > 1$ often referred to as a confidence contour). This confidence interval gives the probability $1 - \gamma$ (confidence level) of containing the true parameter $\boldsymbol{\alpha}$. The values for the test statistic in one and two dimensions referring to a certain confidence interval are given in Table 3.1 [35]. So an interesting point for one-dimensional likelihood scans is the 1σ confidence interval, given by $-2 \cdot \Delta\log(\mathcal{L}) = 1$.

Table 3.1: Values of the test statistic for different confidence levels according to Wilk's theorem for one and two-dimensional likelihood scans [35].

Confidence Level $(1-\gamma)$	n=1	n=2
68.27% (1σ)	1.00	2.30
90%	2.71	4.61
95.45% (2σ)	4.00	6.18
99%	6.63	9.21

3.3.5 Asimov Dataset

It is necessary to test the sensitivity of the analysis before actually performing the analysis. This is done by using an artificial data set, referred to as the Asimov data set, instead of the measured data [36]. The Asimov dataset is constructed by assuming true parameter values for $\boldsymbol{\theta}$, in the MC dataset. By fixing these values, the event numbers per bin in the Asimov dataset are calculated, adding up all events from all flux models. From that, the data histograms are created. The Asimov event numbers per bin can have non-integer values, which is not a problem in the likelihood calculations. The constructed Asimov dataset does not contain statistical fluctuations and is ideal for performing sensitivity studies for new analyses.

3.3.6 Combining Datasets of Different Experiments

For combining the datasets of different experiments, here ARCA and IceCube, the datasets have to be statistically independent [36]. For each dataset i, an individual likelihood functions $\mathcal{L}_i(\boldsymbol{\theta_i}, \boldsymbol{\eta_i} \mid d)$ is defined, where $\boldsymbol{\theta_i}$ denotes the parameters common in all datasets (e.g., flux model parameters), and $\boldsymbol{\eta_i}$ refers to the dataset-specific nuisance parameters.

The full likelihood function is then given by the product over all likelihood functions of the different datasets [36]:

$$\mathcal{L}(\boldsymbol{\theta} \mid d) = \prod_i \mathcal{L}_i(\boldsymbol{\theta_i} \mid d) \tag{3.9}$$

The maximum-likelihood method is then applied as in the single-detector case by minimizing the combined negative log-likelihood. Parameters shared between datasets, in particular the physics parameters of the flux model, can be more tightly constrained through the joint fit. Dataset-specific nuisance parameters can be included independently for each detector; however, unless they are correlated or constrained by common priors, their constraints are not significantly improved by the combination.

With this approach, the analysis binning for the different detectors can differ. The binning enters only when constructing the likelihood function. Once the likelihoods are defined, their combination and subsequent minimization are independent of the chosen binning. This method is used within this thesis to combine the IceCube and ARCA detectors in a galactic analysis. Both software used within this thesis, NNMFit and PyFF, can handle joint detector fits.

3.4 Software for Analyses

As mentioned before, for the different analyses performed within this thesis, different software frameworks are used. The diffuse galactic analysis uses the NNMFit (NewNuMuFit) software framework, and the diffuse all-sky analysis uses the pyFF (pyForwardFolding) software framework.

NNMFit is an established tool for diffuse analyses in the IceCube collaboration. It efficiently handles the forward-folding likelihood fit with a back-end on the `aesara` package [38]. Diffuse galactic analyses with IceCube could already be performed within this framework [39]. This thesis aimes to process KM3NeT simulated events for galactic analyses and perform sensitivity studies for joint IceCube-ARCA galactic analyses

The pyFF framework [23] is the modernist version of NNMFit. Its back end is the `JAX` package [40], which allows for the efficient handling of the forward-folding likelihood fit. It is important to note that pyFF is an open-source framework accessible to all collaborations on GitHub. It has not been used in any diffuse analyses before. This thesis tests it by performing a diffuse all-sky analysis with ARCA. The diffuse all-sky analysis also serves as a proof of concept for using the framework for the ARCA detector.

One challenge of using one framework for different detector datasets is that all MC simulations must be implemented according to one common weighting definition. As both frameworks, NNMFit and PyFF, were originally developed for analysing IceCube data, both use the IceCube definition of a baseline weight w_{baseline}. The baseline weights correct for the simulation spectrum, and therefore follow a flat spectrum. From these baseline weights, all j flux models with flux Φ_{flux} are calculated: $w_j = w_{\text{baseline}} \cdot \Phi_{\text{flux}}$. The number of events per bin and per second is determined by summing all the flux weights in bin i: $\mu_i = \sum_j^N w_{ij}$. The simulated detector lifetime can then be scaled up or down, as the number of events per bin per second is multiplied by the simulated detector livetime $t_{\text{detector-lifetime}}$. The weights in NNMFit are given in units of GeVcm^2sr.

In order to achieve the same weighting definition for the ARCA21 detector, one has to divide the flux weights $w_{\text{flux, ARCA21}}$ by the detector lifetime to have the weights per

second. Multiplying the flux weights with a factor 10^4 ensures the same unit as used by NNMFit: $w_{\text{baseline}}^{\text{ARCA21}} = 10^4 \cdot w_{\text{flux, ARCA21}}/t_{\text{detector-livetime}}$.

For the ARCA115 detector, the baseline weight is computed by $w_{\text{baseline}}^{\text{ARCA115}} = 10^4 \cdot w_{\text{flux, ARCA21}}$ as the simulation is not performed on a run-by-run basis.

The correct implementation of the binning for ARCA can be validated by computing the event numbers, assuming a specific flux model with NNMFit. They can be compared to the event numbers computed with a KM3NeT framework.

3.5 Methods for Diffuse Analysis

As explained in subsection 3.3.2, both analyses performed within this thesis are based on the forward-folding method. In general, the handling of a diffuse and galactic analysis is quite similar. Differences between both analyses are explained in subsection 3.5.4. The MC events and also the data events later have to be preprocessed with different cuts, as explained in the next subsections. Another important step is handling the background and systematic uncertainties of the detector. If all these parameters are set, sensitivity studies, fitting the Asimov dataset, are performed. For determining the statistical significance of such fits, likelihood scans are performed as described in subsection 3.3.4. In an analysis, the last step would be to fit the data events to the modeled flux. This, however, will not be covered within this thesis.

3.5.1 Event Selection

Not all events measured in the detector are suitable to be used in an analysis. Within this analysis, only up-going track events should be used as they have a good pointing resolution. So the events have to fulfill criteria on the track quality, e.g., a certain number of DOMS are hit, or the likelihood for track reconstruction has to be high enough to qualify the events as a track. It also has to be considered that the direction of the track passing the detector can be mis-reconstructed. So there are still atmospheric muons contained within an up-going neutrino sample.

3.5.1.1 Event Selection - IceCube

IceCube already has a standardized up-going track selection. These tracks are referred to as Northern Tracks [41], as up-going events for IceCube come from the North. This Northern track sample was already used in various analyses [39, 19, 42]. The events go through a chain of various cuts and reconstruction algorithms. In a final level, the high-quality tracks with a zenith angle $\theta > 85°$ are processed by a Boosted

Decision Tree (BDT) to distinguish between mis-reconstructed atmospheric muons and the signal. Each event is therefore labeled with a BDT score how likely it is to be a neutrino. On that BDT score, the events are cut such that a data sample with a neutrino purity of 99.7% remains [41].

3.5.1.2 Event Selection - ARCA

An event selection similar to IceCube's Northern tracks is intended to be used for the ARCA detector. So far, KM3NeT does not have a standard event selection for up-going events.

ARCA21

For ARCA21 diffuse analyses, a BDT that selects high-quality tracks and rejects atmospheric muons has been trained [43]. The BDT score ranges from −1 to 1, where high BDT scores represent a high probability to be a neutrino track (cf. Figure 3.2). The BDT cut has to be optimized for the specific analysis.

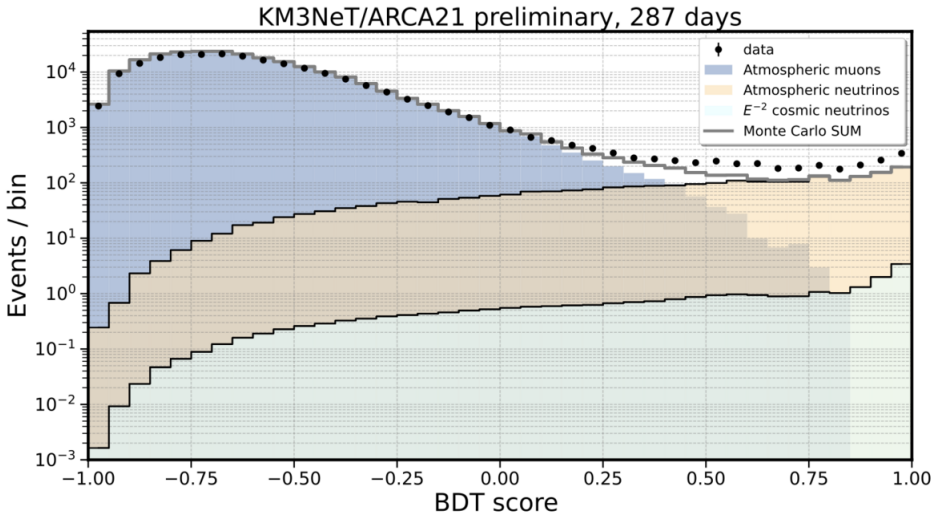

Figure 3.2: Plot created by [43], showing the BDT score distribution of the MC simulated atmospheric muons and neutrinos and data for ARCA21. The number of atmospheric muons (blue) decreases for higher BDT values, whereas the number of neutrinos (orange and green) increases with higher BDT values.

Before applying a BDT cut, some Pre-Cuts are applied. The pre-cuts are $E_{\text{reco}}^{\text{uncorrected}} > 0$ (uncorrected Energy), likelihood > 40 (track-hypothesis likelihood), $dir_z > -0.1$ (z-axis direction, referring to $\cos(\phi)$), $l_{\text{track}} > 100\,\text{m}$ (track length), $log(\beta_0) < -1.5$

(angular error). The pre-cuts reject events that do not have physical values in their reconstructed variables. Additionally, they are first quality cuts for well-reconstructed events, as well as for selecting only up-going events.

From the previous all-sky analysis in KM3NeT there are also some recommendations for first level cuts additionally to cutting data at a specific BDT-score: likelihood > 50 (track-hypothesis likelihood), Tracklength_IT2 $> 100\,\mathrm{m}$ (distance of the vertex and last emitted photon), Tracklength_IT3 $> 100\,\mathrm{m}$ (distance of first emitted photon and last), $N_{DOMS} >= 5$ (number of triggered DOMS), $log(E_{reco}) > 2.7$ (reconstructed Energy), and $\theta > 85°$ (zenith angle). They can be optimized within the individual analysis, but within this thesis, they are just applied as suggested. Still, the BDT-cut has to be determined for the specific analysis. This is discussed in section 4.2 and section 5.2.

ARCA115

The ARCA115 event selection applies first some Preselection cuts to select only physical values of the reconstructed variables and to reject the majority of atmospheric muons. Cuts applied to guarantee physical values in the reconstruction variables are likelihood > 0, tracklength > 0, and $\beta_0 > 0$. To account only for up-going events, the preselection $dir_z > 0$ is applied. An energy cut at $E_\nu > 300\,\mathrm{GeV}$ is applied to account only for high-energetic neutrino events. Additionally, preselection quality cuts are applied, $N_{DOMS} >= 2$, and the distance between the Cherenkov hits closest and furthest from the interaction vertex has to be larger than 200 m.

After preselection, a BDT cut can be applied. For that, a BDT is trained to select well-reconstructed tracks [44]. The muon track reconstruction quality should have an error of less than one degree. The higher the BDT cut, the more atmospheric muons are rejected by selecting only tracks of such high quality and only up-going events. The BDT score distribution for the BDT score $0.63 < BDT < 1$ is shown in Figure 3.3.

The selection of a BDT cut is again chosen for the individual analysis. The BDT cut selection for the ARCA115 event selection is discussed in section 4.2.

3.5.2 Atmospheric Muon Handling

Even after applying cuts, there are mis-reconstructed atmospheric muons left within the dataset. To handle the muon contamination, they are fitted as a flux component within the analysis.

A simple solution is fitting a normalization to the simulated atmospheric muon events. The main problem with that method is that after the event selection, there is only a small number of simulated atmospheric muons left. An example is shown in Figure 3.4, where the muon histogram for ARCA21 after the event selection is shown. The MC

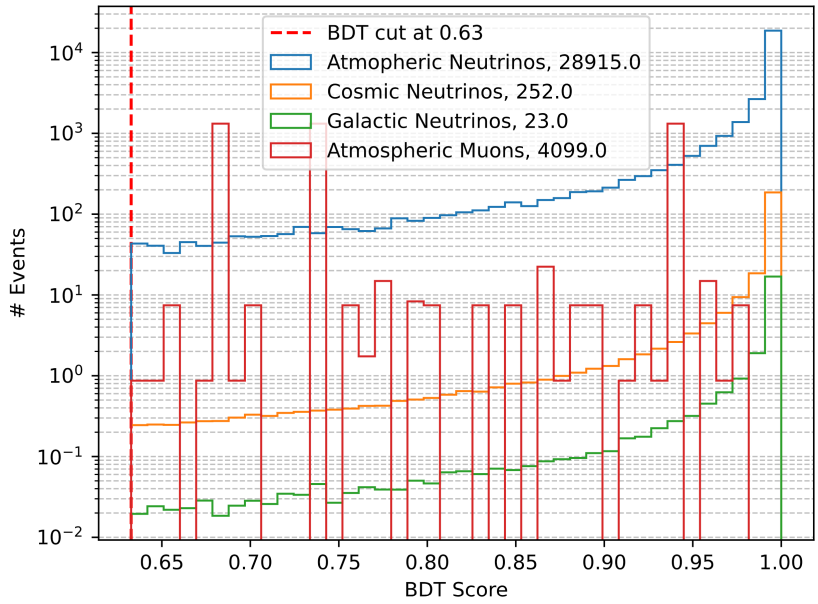

Figure 3.3: BDT score distribution of the ARCA115 MC simulation, weighted for different flux models. This plot shows only the BDT distribution for BDT > 0.63, referring to a purity of 80%.

statistic per bin is therefore not sufficient to account for the muon distribution per bin. This is shown in the plot, as bins with a high muon event number are next to a bin without any muon contribution. In reality, one would expect a rather smooth transition between the single bins.

The simplest approach to accounting for atmospheric muons in the reconstructed data is to add the muon histogram to the overall expected events. More sophisticated methods of building a muon template are also available. One commonly used approach is to create templates from simulated muon events using kernel density estimation (KDE). In this method, each weighted Monte Carlo (MC) event is treated as a smooth kernel, i.e., a localized probability density function (PDF), centered at the event's position in observable space. This results in a continuous estimate of the event density. The expected event counts for the template are obtained by integrating this density over the volume of each analysis bin. Each MC event, therefore, contributes fractionally to multiple bins, according to how much its kernel overlaps with the bin boundaries. In this procedure, the total number of events in the histogram must be conserved.

One method that is planned to be explored in the future involves building atmospheric muon templates using normalizing flows. These are generative models based on neural networks that learn a fully normalized probability density function in a potentially high-dimensional observable space. This space may include zenith, energy, and BDT score,

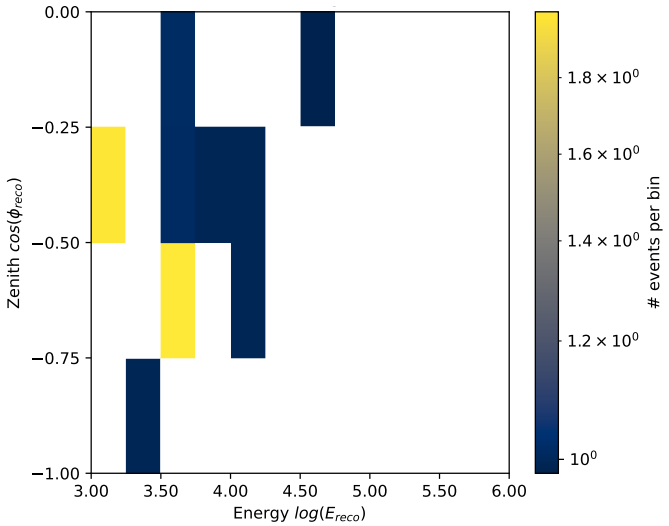

Figure 3.4: This plot shows the atmospheric muon distribution over a zenith and energy binning for the ARCA21 detector after an event selection. The colours account for the weighted number of atmospheric muons contained in the simulation.

for example. The resulting density is integrated over the analysis bin to obtain the expected number of events, in a process similar to that used for KDE-based templates. The advantage of this method is that it can capture more complex correlations between observables. These methods can be used to create a smoother muon template.

3.5.3 Detector Systematics

There are various detector systematics that can be considered. Within this thesis, only detector-related systematic uncertainties for the ARCA detector were implemented in pyFF. KM3NeT provides Monte Carlo simulations in which selected systematic parameters are varied. Currently, datasets with modified water absorption lengths and modified PMT quantum efficiencies are available.

The absorption length is the mean distance that a Cherenkov photon travels in seawater before it is absorbed. An increase in the absorption length leads to a higher photon survival probability, meaning that more photons reach the optical modules. Consequently, the detected light yield and therefore the detection efficiency increase. This effect becomes more pronounced the greater the distance between the photon emission point and the PMTs.

PMT quantum efficiency describes the probability that a photon incident on the PMT photocathode will produce a photoelectron. An increase in quantum efficiency leads

directly to a higher number of detected photoelectrons for a given number of incident photons. The effects of the absorption length and quantum efficiency are statistically correlated because both parameters primarily influence the total light yield detected.

This thesis includes both systematic uncertainty parameters within the ARCA analysis. To achieve this, analysis histograms with varied systematic parameters can be calculated using MC simulation datasets with changed uncertainty parameters. By injecting flux parameters, an Asimov dataset is obtained that determines the number of events per bin and per second. One disadvantage of this method is that the flux parameters have to be fixed before knowing the best-fit parameters.

The event numbers per bin for every MC dataset can be plotted depending on the variation of the systematic parameter, as shown in Figure 3.5. This is done for every analysis bin. The plot for one example bin shows the varied quantum efficiency. 100% quantum efficiency refers to the MC dataset without a systematic parameter variation. It is shown that the number of neutrino events decreases with lower PMT quantum efficiency. This is expected, as the neutrinos can be better detected when the signal strength increases. Additionally, the number of neutrino events increases linearly with the quantum efficiency. Therefore, a linear fit is performed, also accounting for the uncertainties of the event numbers per bin. With that, the gradient ∇ in every analysis bin is determined.

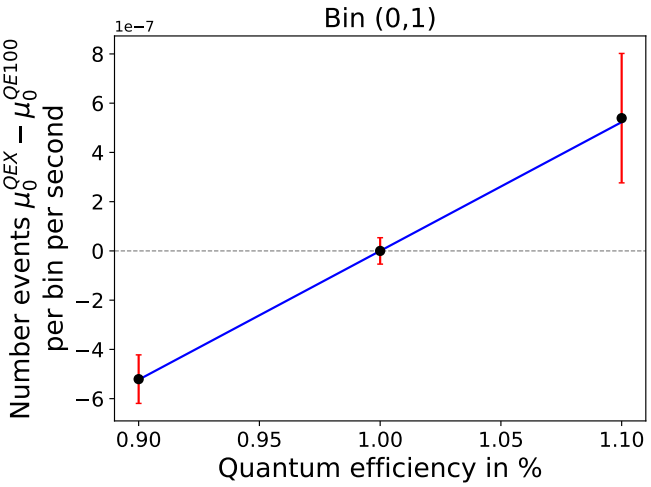

Figure 3.5: Example fit of the varied quantum efficiency of ARCA21 in one bin. The event numbers per bin and second are plotted for each simulation of the varied quantum efficiency (QE90, QE100, QE110), where the baseline MC simulation QE100 is subtracted. The linear fit (blue line) is forced to go through QE100 and accounts for uncertainties in the histogram (red error bars).

These gradients can be used to account for systematic uncertainties in the analysis histogram μ_0. To the analysis histogram, a factor is added, consisting of a new analysis fit parameter α, for every uncertainty parameter, and the gradient:

$$\mu = \mu_0 + (\alpha \cdot \nabla + y) \tag{3.10}$$

With that, the analysis histogram including systematics μ is obtained. Additionally, it can account for the y-intercept y in the gradient fit, but within this analysis, these values are set to $y = 0$. This is chosen, as the analysis fit should recover the MC dataset without systematics, when injecting $\alpha = 0$.

3.5.4 Differences All-Sky Diffuse and Diffuse Galactic Analysis

The general analysis method is the same for an all-sky and galactic analysis. However, they differ in the number of modeled fluxes used. In the galactic analysis, the galactic flux model is added to the analysis, and the diffuse astrophysical flux becomes a background. The diffuse astrophysical flux is approximately isotropic over the sky. The only angular dependence is in the zenith angle of the incoming background. That is why the all-sky analysis can be performed in local coordinates, and the events are binned in energy and zenith. To be able to identify astronomical objects, like the galactic plane, the origin with respect to the sky of the incoming neutrinos becomes important. Consequently, the galactic analysis needs to be performed in equatorial coordinates. Thus, the galactic analysis uses a three-dimensional binning: energy, declination, and right ascension.

As the right ascension is the most sensitive angle distribution for the galactic plane, due to the characteristic shape, a fine binning is important on that axis. In former IceCube Northern track analyses 180 right ascension bins were used [41]. Introducing a further binning axis gives rise to the problem of decreasing MC statistics per bin. To take the MC statistic into account for an analysis, the SAY likelihood is used (c.f. subsection 3.3.3). With that, the performance of different bin numbers in the analysis can be compared.

A method to not decrease the MC statistic by introducing a third binning axis in the galactic analysis is to use oversampling. This is only needed for the galactic fits and is explained in the next subsection.

3.5.5 Coordinate Systems

Before discussing the topic of oversampling, it is important to explain the fundamental concept of how the coordinate systems around the neutrino telescopes are chosen.

Within this thesis, two neutrino detectors are considered: IceCube, located at the South Pole, and ARCA, located in the Mediterranean Sea. Usually, the direction of neutrinos measured within the detector is described in the local coordinate system of the detector, centered on the detector. For that, azimuth ranging from 0 to 2π, and zenith θ ranging from 0 to π are used. The zenith measures the angular distance perpendicular to the vertical axis going through the center of Earth and the center of the local coordinate system. So the horizon is located at $\theta = \pi/2$. Also, the time of the incoming event is known. This becomes important as the local coordinate system is rotating with the Earth.

To associate the direction of neutrino events with the location of astronomical objects, the equatorial coordinate system is used. This coordinate system is based on the center of the Earth. The declination δ describes the angular distance perpendicular to Earth's equator, ranging from $-\pi/2$ to $\pi/2$ [45]. So the equator is located at $\delta = 0$ and the South pole at $\delta = -\pi/2$. The right ascension (RA) α measures the angular distance in the eastern direction on the equator, ranging from 0 to 2π. The equatorial coordinate system does not rotate with the Earth and is fixed to the mean equinox of a standard epoch, usually J2000. As the Earth's axis undergoes small motions due to precession and nutation, this is not an exact definition; however, for the lifetime of a neutrino telescope, these effects are negligible.

The coordinate transfer for a neutrino event from (zenith, azimuth) to (declination, RA) is time independent for the declination angle. Neutrino events coming from a certain direction in the local coordinate system always have the same declination angle, independent of the Earth's rotation. To get the right ascension angle, the arrival time of the neutrino is also important. Due to Earth's rotation, events coming from the same direction in local coordinates at different times can have different right ascension angles. The events are then spread over a band parallel to the equator with the same declination angle. This concept is important when discussing oversampling for the KM3NeT/ARCA and IceCube detectors.

3.5.6 Oversampling

The number of events simulated in MC is limited. Thus, only a small number of events in the simulation are simulated, arriving from the direction of the galactic plane. The simulated events have an arbitrary time stamp and a specific direction in local coordinates. To identify whether the event comes from the galactic plane, equatorial coordinates are used. As explained in subsection 3.5.5, the coordinate transfer for the declination is time independent and for the right ascension is time dependent. To generate more MC events from the galactic plane, one can use different time stamps for the same event in local coordinates and oversample over the right ascension axis. An example of that is shown in Figure 3.6, where for one MC event, different arrival

times for a detector located approximately at the ARCA position are assumed. The event arrival direction is then transferred from local to global coordinates.

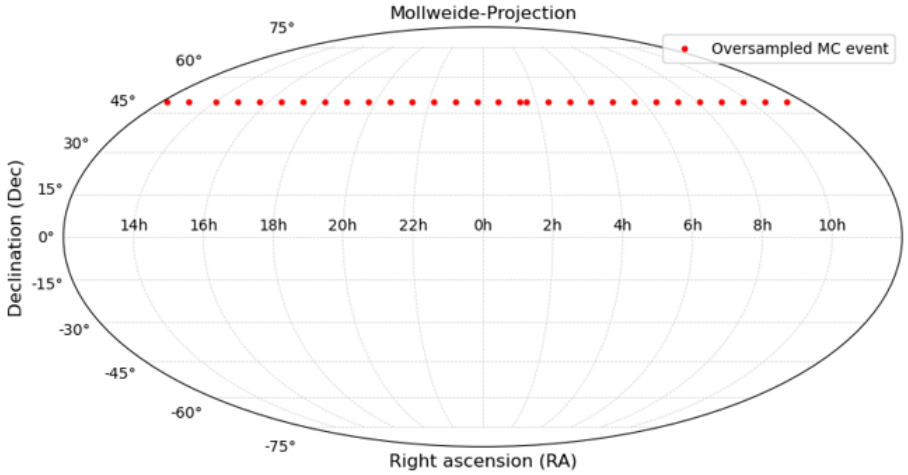

Figure 3.6: Mollweide projection of the Earth, showing oversampling of one MC event in right ascension by assuming different arrival times. The declination direction is unaffected.

Therefore, only the right ascension axis can be oversampled. While their right ascension is randomised, the declination and all other properties of the MC events remain unchanged. This approach increases the MC statistic per bin in the galactic analysis.

However, the oversampled MC events are not statistically independent. Consequently, any statistical uncertainties or potential biases present in the original Monte Carlo sample are propagated across all right ascension bins. In particular, fluctuations or mismodelling in the Monte Carlo simulation can affect multiple bins simultaneously, leading to correlated uncertainties that are not accounted for in the analysis.

There are methods to mitigate these limitations. One approach is binning optimization using end-to-end optimized summary statistics, as described in [46], which allows for a greater number of observables to be included. In this framework, a neural network is trained to compress multiple event observables into a low-dimensional summary statistic optimized for the relevant physics parameters. This enables a greater number of observables to be included in the analysis while ensuring there is a sufficient number of MC events per bin. This allows adding the right ascension axis to the observables without oversampling.

4 Results Diffuse Galactic Analysis

This chapter presents the current results of the sensitivity studies for the diffuse galactic analysis, with a joint IceCube and ARCA fit. The goal of the diffuse galactic analysis is to determine sensitivities for a combined IceCube and ARCA analysis. It currently includes only the neutrino MC dataset from both detectors, and within this thesis, only Asimov fits were performed. The sensitivity studies for the galactic fit within this thesis do not include a muon background or systematic uncertainties. The analysis was performed with the ARCA21 MC dataset and the ARCA115 MC dataset described in section 3.2. These were implemented into the NNMFit framework, which was used for this analysis.

4.1 Proof of Concept in NNMFit

It is particularly important to check that the weighting is correctly applied to the newly implemented ARCA dataset. To do this, event numbers are calculated using a certain flux assumption and compared to previous analyses in KM3NeT.

A KM3NeT analysis using the same ARCA21 MC dataset is the galactic ridge analysis from 2024 [43]. For that, the event numbers for 287 days of detector livetime are calculated. To these events, the event pre-cuts and up-going selection is applied, but no BDT cut. Within that work, the cosmic neutrino flux is assumed to be a power law with a spectral index $\gamma = 2$ and a normalization of $\Phi_{\text{astro}} = 1.2$. So from the cosmic flux, 24.8 neutrino events are expected for ARCA21. For the atmospheric background flux estimation, the Honda flux model for conventional atmospheric neutrinos and Enberg model for prompt neutrinos were used. These predict 2504 conventional atmospheric and 17 prompt neutrino events (cf. Table 4.1).

The cosmic neutrino event number is exactly reproduced in NNMFit with the same event selection and flux assumption. For the atmospheric modeling, instead of Honda, MCEq models are used (cf. section 3.1). Small deviations are expected. The MCEq model predicts 2442.5 atmospheric neutrino events.

For the ARCA115 MC dataset, the same event number checks are performed. For that, the event numbers obtained in [44] are used. As the ARCA115 detector has no live time yet, the live time can be set arbitrarily. For ARCA115, also a power-law

Table 4.1: Neutrino event numbers after pre-selection cuts for ARCA21 (287 days livetime) and ARCA115 (1 year livetime), assuming an E^{-2} cosmic spectrum and using MCEq and Honda for atmospheric modelling.

	number of events	
	ARCA21, 287 **days**	**ARCA115,** 1 **year**
atm. neutrinos	2,521 (Honda)	33,740 (Honda)
	2,442 (MCEq)	32,339 (MCEq)
cosmic neutrinos	24.8	85
atm. muons	$2.3 \cdot 10^5$	$7.8 \cdot 10^5$

spectrum with a spectral index $\gamma = 2$ and $\Phi_{\text{astro}} = 1.2$ is assumed, giving 85 cosmic neutrinos per year. This is recovered in the NNMFit weighting. The atmospheric modeling with the Honda model gives around 33,740 atmospheric neutrinos, which is approximately the same for the MCEq modeling, giving 32,339 atmospheric neutrinos (cf. Table 4.1).

So the weighting for ARCA21 and ARCA115 is correctly implemented. With that, also the galactic component is implemented, accounting for the galactic neutrino flux modeled by the CRINGE model (cf. section 2.3).

4.2 BDT Cut Optimization for Diffuse Galactic Analysis

For the IceCube experiment, the northern track selection with a purity in the neutrino sample of 99.7% is used, so no further optimisations are required. For ARCA, a simple initial approach used in the galactic sensitivity study is to obtain a sample with $> 97\%$ neutrino purity. Another criterion for selecting the BDT cut is to ensure that no high-energy atmospheric muons remain in the event sample. However, the BDT cut must be chosen so that it does not result in too much sensitivity being lost from the event sample. This is why, in the first step, the relationship between sensitivity, referring to the signal strength (number of neutrino events remaining in the dataset), and purity, referring to the effectiveness of the BDT cut (muon contamination in the dataset), is investigated. Then, the energy distribution of the remaining atmospheric muons is examined.

The BDT distribution of the different flux components for ARCA21 is shown in Figure 3.2. Using this BDT, the purity and efficiency of a BDT cut are studied for ARCA21, as shown in Figure 4.1. Given the requirement for a neutrino sample with a purity greater than 97%, the efficiency for the number of galactic events remains constant between 97% and 98% purity. This is why a cut at 98% purity (indicated by the red dashed line) is chosen. Checking the energy distribution of the remaining

atmospheric muons (cf. Figure 4.2) shows that only two simulated muons remain in the energy range $E > 10^3$ GeV. Therefore, the BDT cut of $BDT > 0.67$, which gives a purity of 98%, is chosen for the galactic analysis. The MC dataset after event selection in ARCA21 therefore contains 19 cosmic neutrinos, 1.4 galactic neutrinos, 827 atmospheric neutrinos, and 13 atmospheric muons within a detector livetime of 287 days.

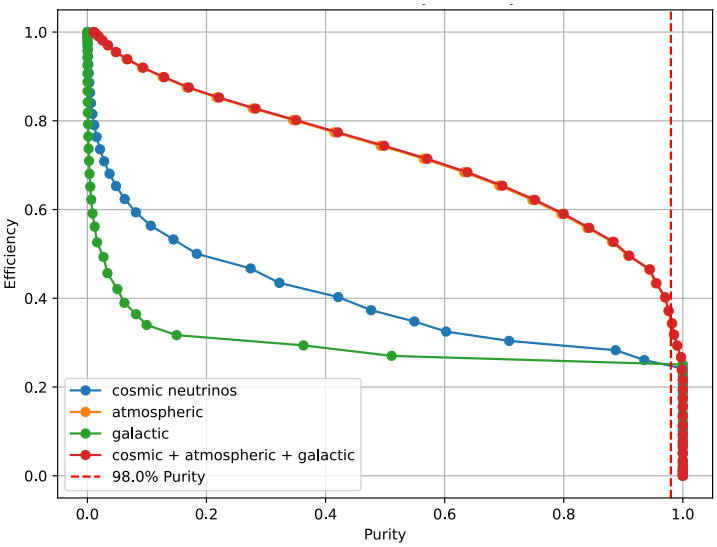

Figure 4.1: This plot shows the relation between purity and efficiency, for choosing different BDT cuts in ARCA21. The different colors indicate the different flux components, where the orange line for the atmospheric neutrino events is behind the red line for all neutrino events. The red dashed line refers to a purity of 98% in the neutrino sample, where a BDT cut of $BDT > 0.67$ is applied.

For the ARCA115 event selection, a specifically trained BDT is used [44]. By iterating over different BDT scores and calculating the purity and efficiency of the neutrino sample, it becomes noticeable that the atmospheric muons are not distributed smoothly over the BDT score. Instead, cutting at a higher BDT score suddenly cuts away several events. This is shown in the purity and efficiency distribution for ARCA115 Figure 4.3, where the distribution is not smooth. The red dashed line indicates the 98% purity mark at a BDT score of $BDT = 0.95$, which has the same purity as the ARCA21 dataset. The energy distribution of the atmospheric muons remaining after this BDT cut shows that they all have an energy greater than $E > 10^3$ GeV (cf. Figure 4.4). Cutting at a higher BDT would remove all muons in the dataset. With that, describing the atmospheric muon background in MC would become difficult. Therefore, it is preferable to retain this muon contamination in the ARCA115 MC dataset.

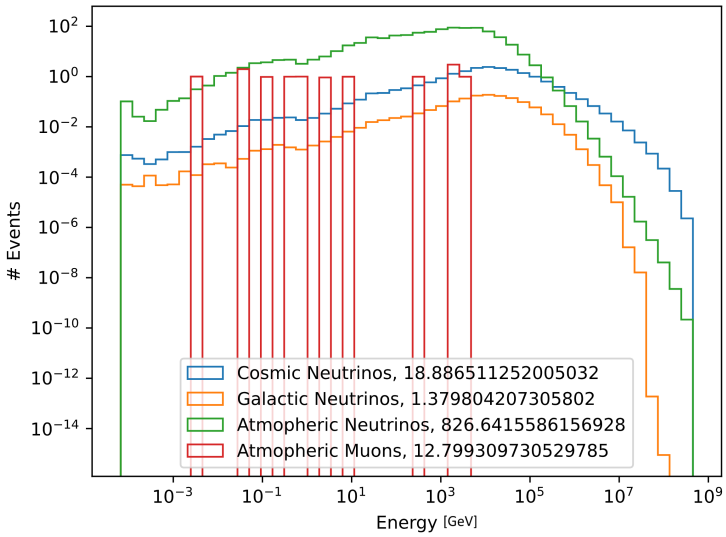

Figure 4.2: Energy distribution of events surviving the ARCA21 BDT cut, giving a purity of 98% (BDT cut at 0.67). Within the event selection remain about 19 cosmic neutrino events, 1 galactic event, 827 atmospheric events, and 13 atmospheric muon events.

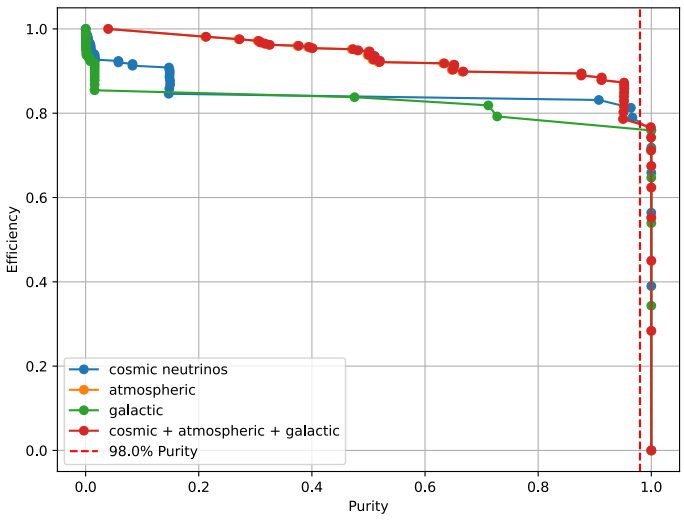

Figure 4.3: This plot shows the relation between purity and efficiency, for choosing different BDT cuts in ARCA115. The different colours indicate the different flux components. The red dashed line refers to a purity of 98% in the neutrino sample, where a BDT cut of $BDT > 0.95$ is applied.

After performing the event selection for 1 year of livetime in ARAC115, there are 227 astrophysical, 21 cosmic, 24, 782 atmospheric neutrinos, and 23 atmospheric muons left in the MC dataset.

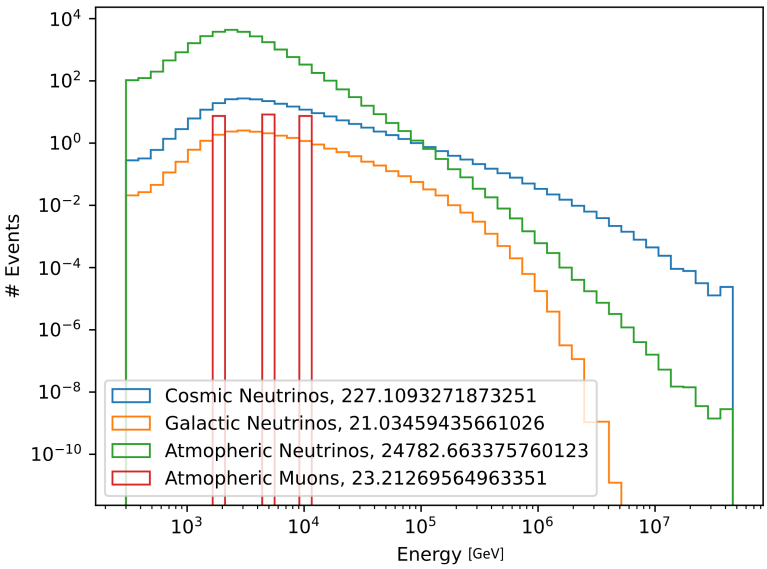

Figure 4.4: Energy distribution of events surviving the ARCA115 BDT cut, giving a purity of 98% (BDT cut at 0.95). The concrete event numbers are shown in the legend for each flux component.

4.3 Likelihood Scans using Poisson Likelihood on the Galactic Normalization

After fixing the event selection, first, LLH-scans for a sensitivity study in MC are performed. The scans are used to compare the performance of the different detectors. There is no atmospheric muon handling or systematic treatment included yet. After performing this sensitivity study, it was noticed that there is a factor of two missing for the scans shown in this section. However, within this thesis, only statements for comparing the detectors are made. The absolute significance of the analysis, which is not correctly implemented, will not be regarded.

The most interesting parameter for a galactic analysis is the galactic normalization. For the Asimiov dataset, the injected normalization of the CRINGE template is set to $\Phi_0^{\text{galactic}} = 1$. This parameter of interest is then scanned to determine the likelihood values. The other free fit parameters in the Asimov dataset are set to $\Phi_0^{\text{astro}} = 1.77$, $\gamma^{\text{astro}} = 2.44$ for the astrophysical flux, and $\Phi_{\text{conv}} = 1.0$, $\Phi_{\text{prompt}} = 0.0$ for the atmospheric flux.

The scans in this section are performed with a Poisson likelihood, using the three-dimensional binning (Energy, Dec, R.A.) $= (50, 33, 180)$. The energy binning is in the range of $10^2\,\text{GeV} < E_\nu < 10^7\,\text{GeV}$, and the right ascension binning $0 < R.A. < 2 \cdot \pi$. The declination binning range differs for KM3NeT $-1 < \sin(\delta) < 0.85$, and for IceCube $-1 < \cos(\delta) < 0.0872$.

4.3.1 Joint Likelihood Scans for IceCube and ARCA21

The first sensitivity study addresses the current status of the ARCA detector. As previously mentioned, the location of the ARCA detector is better situated for galactic analysis for up-going events. However, the volume of the ARCA21 detector is currently approximately ten times smaller than that of the IceCube detector. One question is how sensitive the galactic flux of the ARCA21 detector already is compared to that of the IceCube detector. As a preliminary test, a likelihood scan was performed using the current detector lifetimes: IceCube with 11.67 years, and ARCA21 with 287 days, shown in Figure 4.5.

The sensitivity of IceCube for upgoing events is much higher than for the current ARCA building phase. The 1σ interval for IceCube is determined to be approximately $\Delta\Phi_{\text{galactic}}^{\text{IC,12.67}} \approx 1.5$. The 1σ intervall of ARCA21 can only be estimated to be 30 times wider than the one for IceCube, as it is not contained within the scanned region. However, it is significantly larger than the IceCube interval. Therefore, IceCube currently dominates sensitivity on the galactic plane. This is demonstrated in Figure 4.6, which shows a combined fit of ARCA21 and IceCube with current

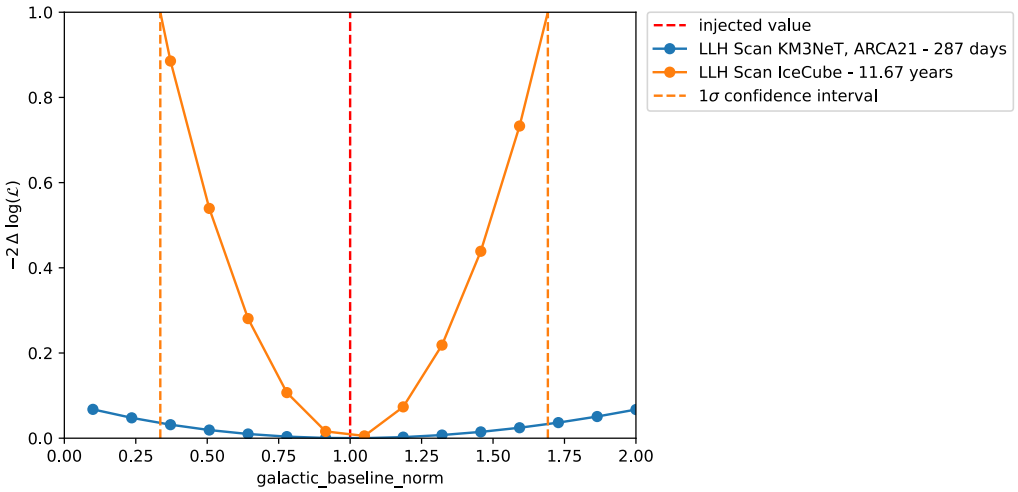

Figure 4.5: Poisson likelihood scan over the galactic normalization in an Asimov test for ARCA21 and IceCube. The current livetimes of IceCube, 11.67 years, and ARCA21, 287 days, are used. The injected value for the normalization of the galactic model is $\Phi_{\text{galactic}} = 1$. The dashed orange line indicates the 1σ confidence interval for IceCube. The 1σ intervall for ARCA21 is not within the scanned region.

lifetimes. The figure shows that ARCA21 improves the significance of IceCube to the galactic plane by only a small amount. Therefore, the current ARCA21 detector has a negligible impact on joint detector studies of the galactic plane.

The actual sensitivity of ARCA21 in comparison to IceCube, independent of the livetime, is compared in Figure 4.7. For that, the livetime of both detectors is set to the same value: 12.67 years. The 1σ confidence interval of IceCube is still smaller than that of ARCA21, but the detectors become more compatible. Despite being around ten times smaller, the ARCA21 detector is almost as sensitive to the galactic plane as the IceCube detector.

4.3.2 Joint Likelihood Scans for IceCube and ARCA115

As the ARCA detector is still under construction, a more realistic comparison can be made between the IceCube detector and the projected first building block of the ARCA115 detector. It is also interesting to consider how sensitivity would improve with a future combination of ARCA115 and IceCube. It is assumed that ARCA115 could be built by around 2028. As shown in Figure 4.8, if ARCA115 is operational by 2028, it will have the same sensitivity to the galactic plane as IceCube after five years of operation. IceCube at that time will have a livetime of a bit more than 20 years.

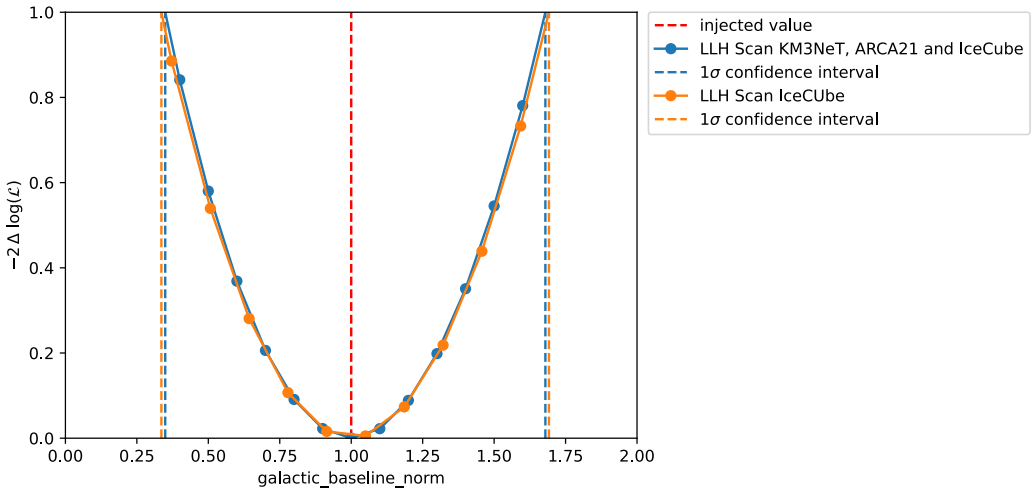

Figure 4.6: Poisson likelihood scan over the galactic normalization in an Asimov test for IceCube and joint IceCube + ARCA21. The current detector livetimes of 11.67 years for ICeCube and 287 days for ARCA21 are used. The injected value for the normalization of the galactic model is $\Phi_{\text{galactic}} = 1$. The dashed orange and blue lines indicate the 1σ confidence intervals for IceCube and IceCube + ARCA21.

Also, the effect of a combined fit of IceCube and ARCA115 is shown. It improves the width of the 1σ confidence interval of the galactic normalization by about 25%. This is expected, as both detectors have the same sensitivities on the galactic plane in that study.

4.4 Likelihood Scans using SAY on the Galactic Normalization

The SAY likelihood accounts for uncertainties due to low MC statistics, as discussed in subsection 3.3.3. To increase the MC statistics, the oversampling method (cf. subsection 3.5.6) is used in the right ascension axis. The right ascension events are oversampled three times. The effect of performing a SAY fit with and without oversampling is shown in Figure 4.9 for IceCube, using the same binning as before: (Energy, Dec, R.A.) = $(50, 33, 180)$. The injected value for the galactic normalization in the Asimov dataset is $\Phi_{\text{galactic}} = 1$, as shown in the Poisson likelihood scan. The scan curve of the SAY likelihood scan without oversampling has its minimum at $\Phi_{\text{galactic}}^{\text{SAY, no overs.}} \approx 0.75$. So it does not recover the injected value. This can occur when the SAY likelihood is used with insufficient MC statistics per bin. It is shown that by increasing the MC statistics per bin by oversampling, the bias in the likelihood scan is smaller. The width of the one sigma interval of the scan using oversampling compared

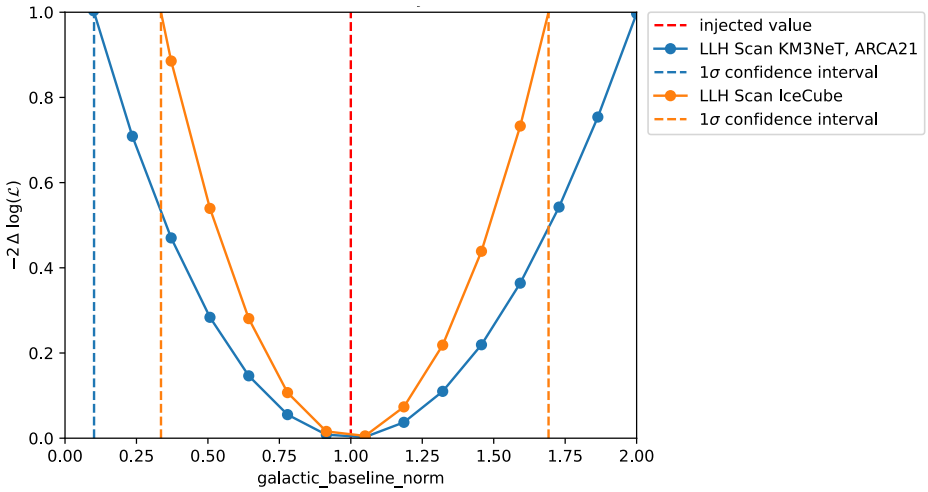

Figure 4.7: Poissonian likelihood scan over the galactic normalization in an Asimov test for ARCA21 and IceCube. The same livetime for both detectors, 11.67 years, is used. The injected value for the normalization of the galactic model is $\Phi_{\text{galactic}} = 1$. The dashed orange and blue lines indicate the 1σ confidence intervals for IceCube and ARCA21.

to the scan using the Poisson becomes larger, as the SAY also accounts for larger uncertainties due to the MC statistic. Another feature of the SAY likelihood is seen, that the likelihood scan with SAY and no oversampling has a smaller 1σ confidence interval than the other two scans shown in the plot.

Using the SAY likelihood for the ARCA21 galactic fits to account for MC statistics shows that the previous binning had too many bins. The injected galactic normalisation value cannot be recovered, even with oversampling. This is because the IceCube MC dataset contains $\sim 13 \cdot 10^6$ MC events. In comparison to that, the ARCA21 MC dataset contains $\sim 3 \cdot 10^6$ MC events, which is about a quarter of the simulated events in IceCube. So a reasonable approach for ARCA21 is to use only a quarter of the bins, as in the IceCube analysis. For that, the number of energy bins and the number of declination bins are halved. However, the right ascension bins can be oversampled, so a reduction on this binning axis is not necessary. The binning used for the galactic normalization likelihood scan with ARCA21 using SAY likelihood is then (Energy, Dec, R.A.) = $(25, 16, 180)$.

The likelihood scans for the ARCA21 detector are shown in Figure 4.10. To scale them up, the likelihood scans are performed using the same livetime as for the IceCube detector, 11.67 years. The plot shows the difference between using oversampling and no oversampling when using the SAY likelihood for ARCA21. As expected, the Poisson likelihood scan is less sensitive to the galactic flux with reduced binning. The behaviour of the SY likelihood compared to Poisson is similar to the IceCube scan, where the

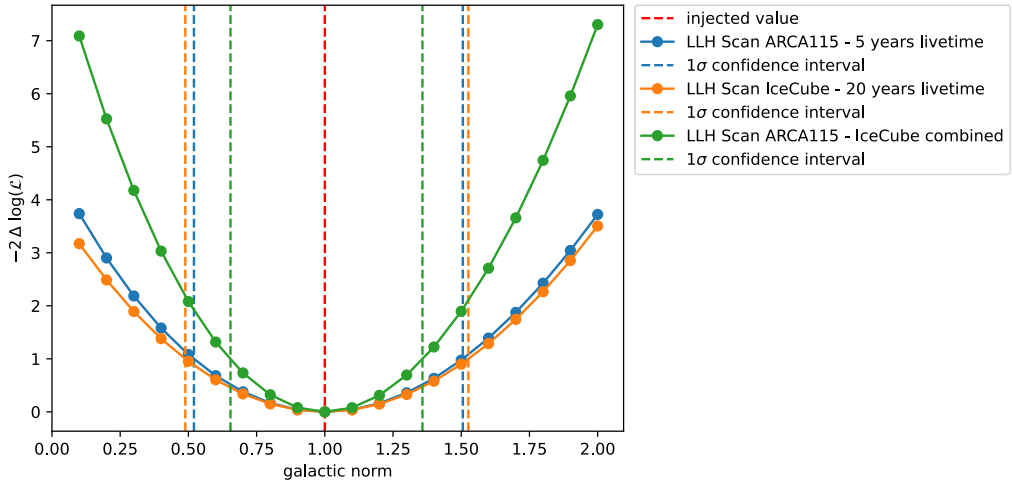

Figure 4.8: Poissonian likelihood scan over the galactic normalization in an Asimov test for ARCA115 and IceCube. For ARCA115, a livetime of 5 years, and for IceCube, a livetime of 20 years is used. The injected value for the normalization of the galactic model is $\Phi_{\text{galactic}} = 1$. The dashed orange and blue lines indicate the 1σ confidence intervals for IceCube and ARCA21. The green likelihood curve shows the joint fit of IceCube and ARCA115.

injected galactic normalisation can only be recovered by including oversampling. The SAY one sigma interval is smaller for the Poisson scan compared to the SAY scan with oversampling.

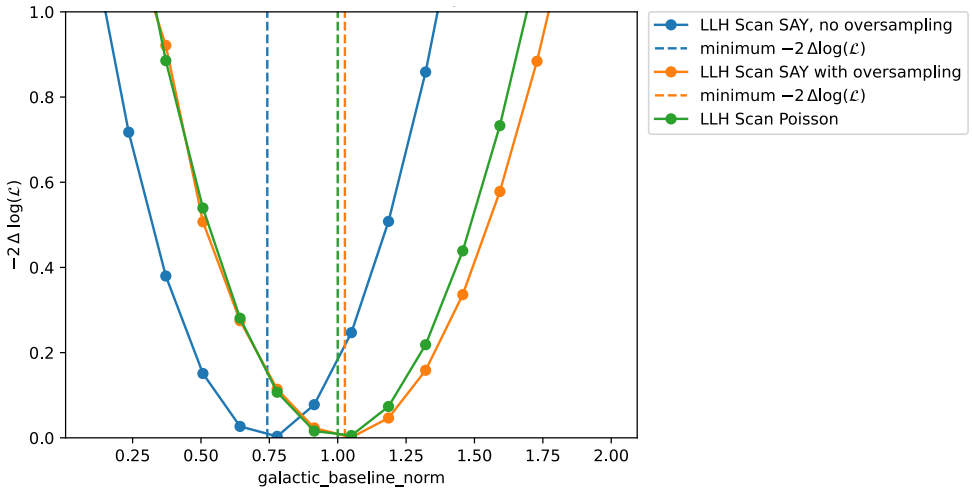

Figure 4.9: Asimov Likelihood scans for IceCube, where the injected value for the galactic normalization is $\Phi_{\text{galactic}} = 1$. The IceCube livetime of 11.67 years is used. The green scan shows the Poisson likelihood. The blue scan uses the SAY likelihood without oversampling. There, the minimum of the scan does not recover the injected value. The blue scan uses the SAY likelihood with oversampling for the right ascension axis.

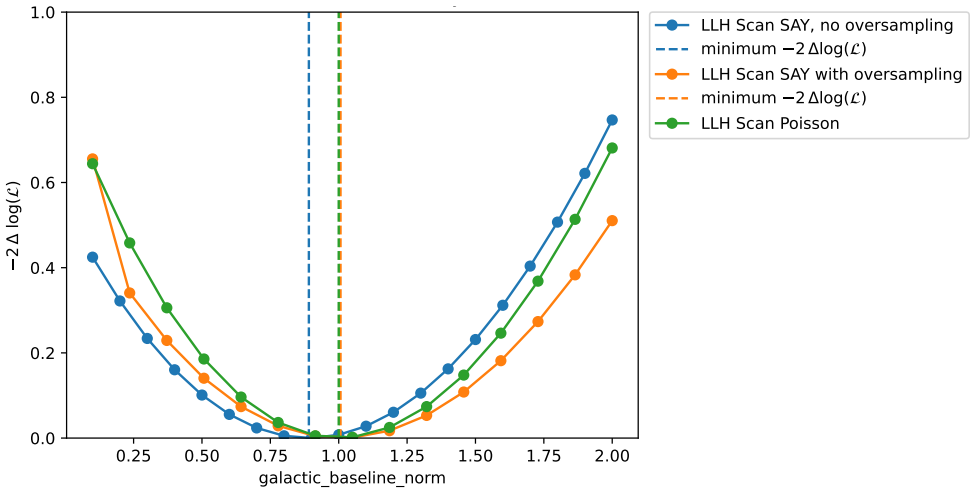

Figure 4.10: Asimov Likelihood scans for ARCA21, where the injected value for the galactic normalization is $\Phi_{\text{galactic}} = 1$. The livetime is scaled to the IceCube livetime of 11.67 years. The green scan uses the Poisson likelihood. The blue scan uses the SAY likelihood without oversampling. There, the minimum of the scan does not recover the injected value. The blue scan uses the SAY likelihood with oversampling for the right ascension axis.

5 Results All-Sky Diffuse Analysis

After performing the joint galactic sensitivity study in the NNMFit framework, a modernised and open-source framework is tested: pyFF. To evaluate the functionalities of pyFF, especially for the ARCA implementation, an all-sky diffuse analysis is performed.

This chapter shows the current status of the all-sky diffuse analysis for ARCA21. This analysis aims to demonstrate the feasibility of implementing an ARCA analysis with background and systematic handling within the PyFF framework. The KM3NeT Collaboration has already performed a Bayesian diffuse all-sky analysis with the ARCA21 detector [47]. This analysis is already unblinded. Additionally, a frequentist analysis is currently set up, using the same data selection [48]. Thus, the diffuse all-sky analysis within this thesis using pyFF is compared to results obtained from the KM3NeT collaboration.

This thesis only considers ARCA21 MC datasets for its analysis, so all fits are performed using Asimov data. This analysis considers the atmospheric muon background (cf. section 5.3). With that, a new approach to event selection is used, which differs from that used in the galactic flux analysis and will be explained in section 5.2. Additionally, detector systematics are implemented, and a new systematics handling method is tested, which differs from those used in other KM3NeT diffuse all-sky analyses.

The entire analysis process is integrated into a single workflow using Snakemake [49]. Snakemake is a workflow management tool that is particularly useful for working with high-performance computing clusters. This makes the entire analysis reproducible and steerable with just two configuration files.

5.1 Proof of Concept in PyFF

The implementation of the ARCA21 MC dataset in the PyFF framework is generally the same as for the NNMFit framework. So the comparison of the correct weighting of the neutrino events is performed as described in section 4.1.

For this analysis, in general, 12 energy bins are used in the energy range $10^3\,\mathrm{GeV} < E_\nu < 10^6\,\mathrm{GeV}$. This is also used in the KM3NeT frequentist all-sky diffuse analyses

and ensures comparability. Within that analysis, no zenith bins are used. However, within pyFF, in principle, a zenith binning can be used.

For the diffuse all-sky analysis, the signal parameters are the astrophysical normalization, Φ_{astro}, and the spectral index γ_{astro}. Therefore, when performing Asimov scans, these are the parameters of interest. When performing one-dimensional likelihood scans, the likelihood curve of the astrophysical normalization is of interest as it shows the uncertainty of the existence of an astrophysical neutrino flux. When performing two-dimensional scans, both the astrophysical normalization and the spectral index are of interest. These likelihood contours also demonstrate the correlation between the two parameters. The ARCA21 Bayesian unblinded analysis obtained best-fit values for the signal parameters: $\Phi_{\text{astro}} = 3.5$, and $\gamma_{\text{astro}} = 3.3$ [47]. Within this analysis, the background parameters are set to $\Phi_{\text{conv}} = 1.0$, $\Phi_{\text{prompt}} = 0.0$, and $\Phi_{\text{muons}} = 1.0$. These best-fit results are chosen in the Asimov dataset for first tests in PyFF, if not otherwise mentioned, for testing the analysis by performing Asimov fits. The neutrino histogram with these expected parameters and 4 zenith bins is shown in Figure 5.1 for the ARCA21 livetime of 287 days. The histogram shows that most neutrino events a contained in the lower energy bins, and the number of neutrino events increases with $\cos(\phi)$ for energies $E_\nu > 10^3.75\,\text{GeV}$.

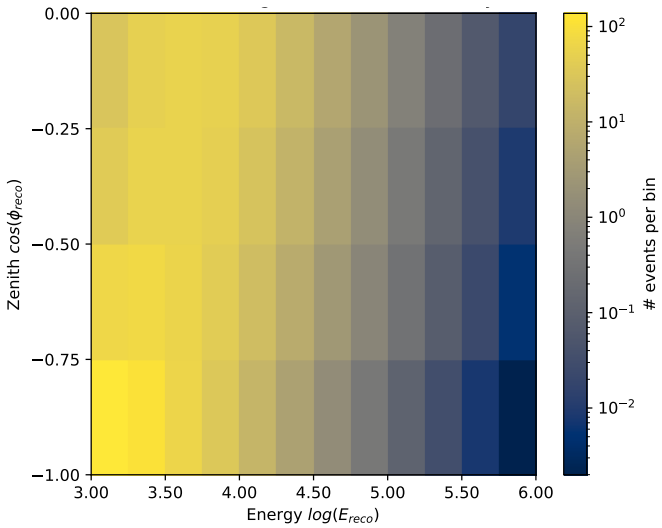

Figure 5.1: The expected neutrino event distribution in ARCA21, binned into 12 energy bins in the range $10^3\,\text{GeV} < E_\nu < 10^6\,\text{GeV}$ and 4 zenith bins, for $-1 < cos(\phi) < 0$. The colorbar shows the number of expected neutrino events per bin. The injected flux parameters are $\Phi_{\text{astro}} = 3.5$, $\gamma_{\text{astro}} = 3.3$, $\Phi_{\text{conv}} = 1.0$, and $\Phi_{\text{prompt}} = 0.0$.

5.2 Event Selection for the All-Sky Diffuse Analysis

The event selection described in subsubsection 3.5.1.2 for the first level cuts is applied for the all-sky diffuse analysis. Only the BDT cut has to be chosen individually for that analysis. For the all-sky analysis, a new, more quantitative approach for optimizing the BDT than presented for the galactic analysis in section 4.2 is applied. This method becomes only applicable as the likelihood scans with atmospheric muon models are now included in pyFF. Within that, the BDT cut for maximal sensitivity on the astrophysical neutrino flux is optimized. The optimization is performed with the included neutrino and atmospheric muon flux models, as the main reason for the BDT cut is the muon background rejection.

For the BDT cut optimization, two methods are tested. One simple method is to choose different BDT cuts, apply them to the MC dataset, and perform Asimov scans with each BDT cut dataset. All these likelihood scans are shown in Figure A.1 in Appendix A. The scanned parameter is the normalization of the astrophysical neutrino flux, as this parameter indicates the sensitivity on the astrophysical neutrino flux. The astrophysical flux normalization for the multiple scans is set to $\Phi_{\text{astro}} = 1$, and the spectral index to $\gamma_{\text{astro}} = 2.37$. It is important to note that within the BDT cut optimization, the prompt and conventional norms are still fitted separately. Additionally, the muon weighting within these likelihood scans is not correctly implemented. As a measurement for maximal sensitivity in this method, the 1σ confidence interval on the log-likelihood curve of the astrophysical normalization is used. The smaller the interval in the likelihood scan of the astrophysical normalization, the higher the sensitivity is reached by applying the BDT cut.

The second method uses a computationally faster approach, using Fisher information. The Fisher information matrix is calculated by

$$F_{ij} = E\left[\frac{\partial \log \mathcal{L}}{\partial \theta_i}\frac{\partial \log \mathcal{L}}{\partial \theta_j}\right] \tag{5.1}$$

The lower limit of the covariance matrix of the fit parameters can be calculated using the Cramér-Rao bound: $\text{cov}\theta \geq F^{-1}$. The variance on the diagonal of that matrix for every parameter gives an estimate of the variance of the likelihood curve width for that parameter. For that, the likelihood curve is assumed to be a quadratic function. With that approach, the widths of different likelihood functions can be compared without performing likelihood scans.

The agreement of both methods is shown in Figure 5.2. As both approaches use the same dataset, the atmospheric muon weighting is implemented incorrectly for both. Therefore, the approaches remain comparable. The uncertainty of the astrophysical normalization using Fisher information is plotted in blue for different BDT cuts.

The 1σ confidence interval of the astrophysical normalization for different BDT cuts is plotted in red. The overall tendency of the optimal BDT cut agrees in both methods. The minimum, referring to the optimal BDT cut, is for both methods between $0.5 < BDT < 0.6$. Only for higher BDT cuts do the tendencies of both methods diverge. But as the agreement of the minimum, which is the interesting point for the BDT optimization, agrees well, the Fisher Information method can be used for the optimization in the future. The advantage is the computational efficiency.

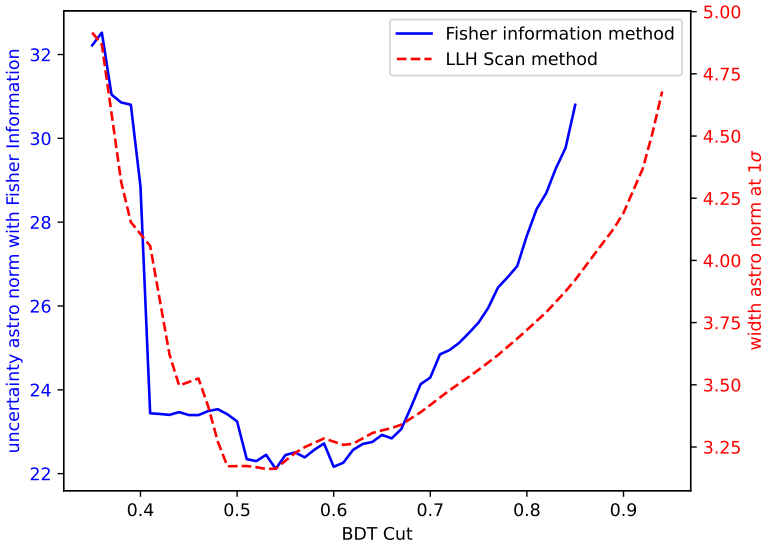

Figure 5.2: BDT cut optimization for ARCA21 with two methods: Likelihood scans and Fisher Information. The blue curve shows the measurement of the uncertainty on the astrophysical normalization using Fisher information. The red curve shows the one sigma interval measured for different BDT cuts.

For the following analysis, a BDT cut of $BDT > 0.5$ is chosen. This is based on the wrong atmospheric muon flux weighting. However, the method using Fisher information is validated. So the BDT cut optimization with correctly implemented atmospheric muons can be checked computationally efficiently by using the Fisher information method shown in Figure 5.3). This plot shows that the sensitivity is highest for $0.4 < BDT < 0.6$. So a BDT cut $BDT > 0.5$ is still reasonable, also with correctly implemented atmospheric muon weights.

The analysis of the Asimov dataset included event numbers obtained using the best-fit parameters from the KM3NeT Bayesian analysis and the described event selection. These numbers are 360 astrophysical neutrino events, 732 conventional atmospheric and 6 prompt neutrino events, and 11 atmospheric muon events. The event distribution over the energy axis for the analysis binning is shown in Figure 5.4.

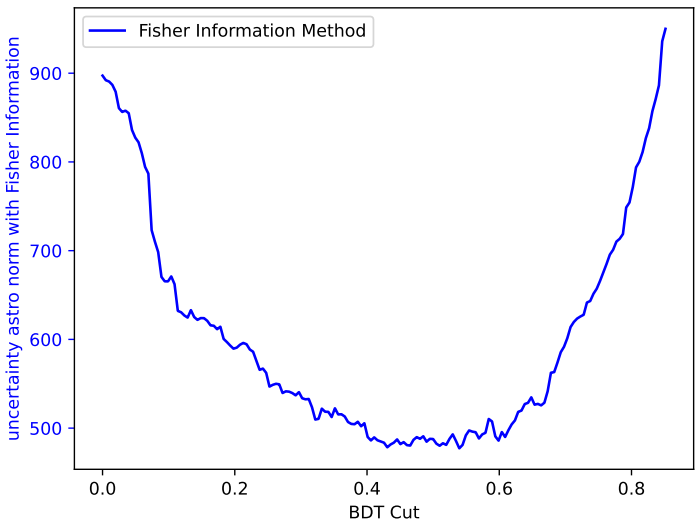

Figure 5.3: BDT cut optimization for ARCA21 by using the Fisher Information. The Fisher information is used to estimate the uncertainty on the astrophysical normalization; therefore, the minimum in the blue curve represents the BDT cut with the highest sensitivity for the analysis. Within this plot, the correct atmospheric muon weighting is implemented.

5.3 Likelihood Scans with Atmospheric Muon Background for ARCA21

As explained in subsection 3.5.2, the atmospheric muon background implemented for ARCA21 is simply the addition of the muon histogram to the expected event histogram, with an additional muon normalization, Φ_{muons}. The muon histogram added in this thesis is shown in Figure 3.4. The event selection described in section 5.2 is applied. As a first proof of concept for adding the atmospheric muon background, the one-dimensional Asimov likelihood scans of the astrophysical normalization are compared, fitting neutrinos only, and additionally including the muon normalization. It is expected that the likelihood curve including only a neutrino model will be slightly above the curve including an atmospheric muon model as well. This is because the total number of background events increases, while the number of signal events remains the same.

The Asimov likelihood scan is shown in Figure 5.5. The likelihood curve, including only neutrinos, is only in a small region for $\Phi_{\text{astro}} < 1$, visibly above the likelihood curve including the atmospheric muon model. The difference of the two likelihood curves is shown in green. Even if a difference is not directly visible, the likelihood contour of the scan, including only neutrinos, is smaller than for the included muons.

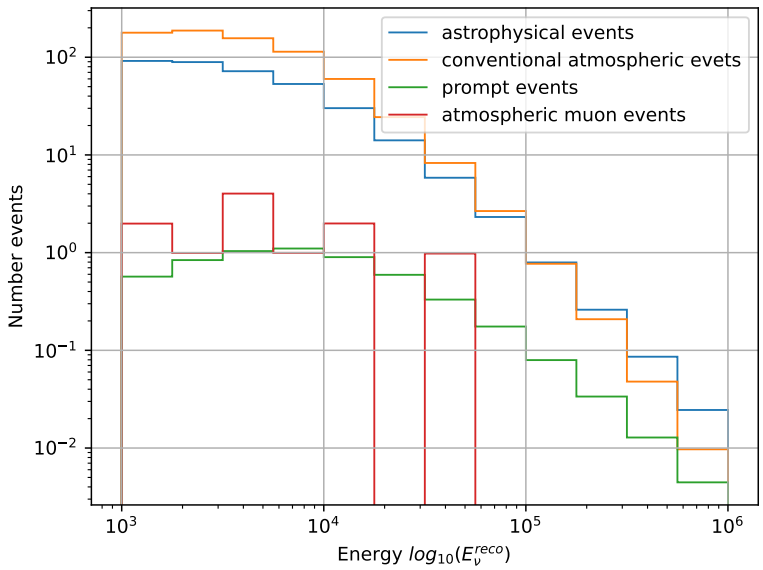

Figure 5.4: Energy distribution of an ARCA21, 287 days, Asimov dataset for different flux components of the all-sky diffuse analysis. This analysis includes astrophysical neutrino events, atmospheric neutrino events (both prompt and conventional), and atmospheric muon events. They are binned into 12 bins in the energy range $10^3\,\text{GeV} < E_\nu < 10^6\,\text{GeV}$. The flux parameters in this Asimov dataset are set to $\Phi_{\text{astro}} = 3.5$, $\gamma_{\text{astro}} = 3.3$, $\Phi_{\text{prompt}} = 1$, $\Phi_{\text{conv}} = 1$, and $\Phi_{\text{muons}} = 1$.

Especially for the likelihood scan close to $\Phi_{\text{astro}} = 0$, the difference between the scans increases. The spike in the green curve is due to a failed fit.

5.4 Combining Prompt and Conventional Atmospheric Flux

Important to note in Figure 5.5 is the non-parabolic shape of the likelihood curve for $\Phi_{\text{astro}} < 3.5$, the injected astrophysical normalization. For that, Figure 5.6 shows the best-fit values of the prompt normalization in each scan point.

The prompt-normalization is fitted in this region to unphysically high values, up to $\Phi_{\text{prompt}} \approx 40$. This is due to a similar power-law description of the astrophysical neutrino flux and the prompt neutrino flux. In the region of a low fixed astrophysical normalization in the likelihood scan, the fitter compensates for that by setting the prompt normalization to higher values. These high prompt normalizations are unphysical, as there is currently no experimental evidence of a prompt flux [12]. The current upper limit on the prompt normalization is set by [50] to $\Phi_{\text{prompt}} = 2.59$ at 90% confidence. However, this significantly reduces sensitivity to the astrophysical

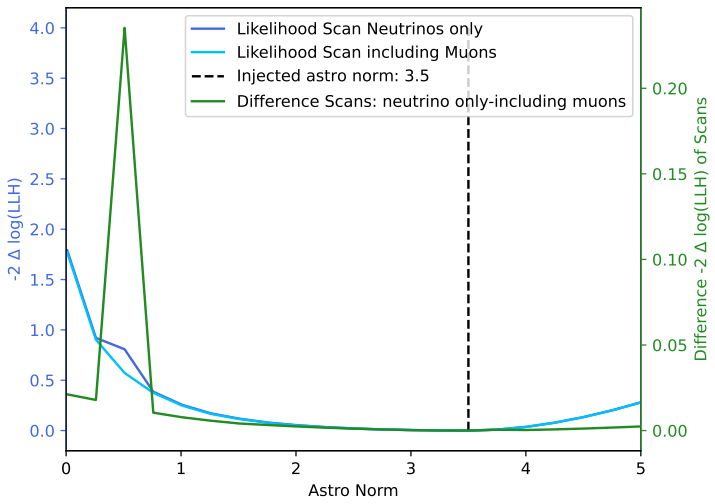

Figure 5.5: Asimov Poisson likelihood scan, comparing the uncertainties on the astrophysical normalization for the fit only with neutrinos and the fit including the simulated atmospheric muons for ARCA21, 287 days livetime. The injected flux parameters are $\Phi_{\text{astro}} = 3.5$, $\gamma_{\text{astro}} = 3.3$, $\Phi_{\text{muons}} = 1.0$, $\Phi_{\text{conv}} = 1.0$, and $\Phi_{\text{prompt}} = 0.0$. The green line shows the difference between the likelihood scan with only neutrinos and one that includes muons. The peak is an outlier because the fit failed.

neutrino flux. Therefore, within this analysis, a single normalization is applied to the conventional and prompt fluxes. This only scales the combined atmospheric models. Another method, which is not used in this thesis, to suppress high fit values on the prompt norm, would be to set a prior on that parameter.

A scan including this combined normalization is shown in Figure 5.7. The slope of the likelihood curve combining prompt and conventional atmospheric flux increases to much higher log-likelihood for $\Phi_{\text{astro}} < 3.5$, than the curve fitting prompt and conventional separately. That is the reason for fitting one combined normalization parameter $\Phi_{\text{conv+prompt}}$ for the conventional and prompt flux components in the further analysis.

5.5 Likelihood Scans with Detector Systematics for ARCA21

The implementation of the detector systematics for ARCA21 is performed as described in subsection 3.5.3. There are two systematic parameters considered for the ARCA detector: absorption length and quantum efficiency. For the absorption length, there are three datasets with varied absorption lengths. One with 90%, 95%, and 110% absorption length of the standard MC dataset. For the quantum efficiency, there exist only two

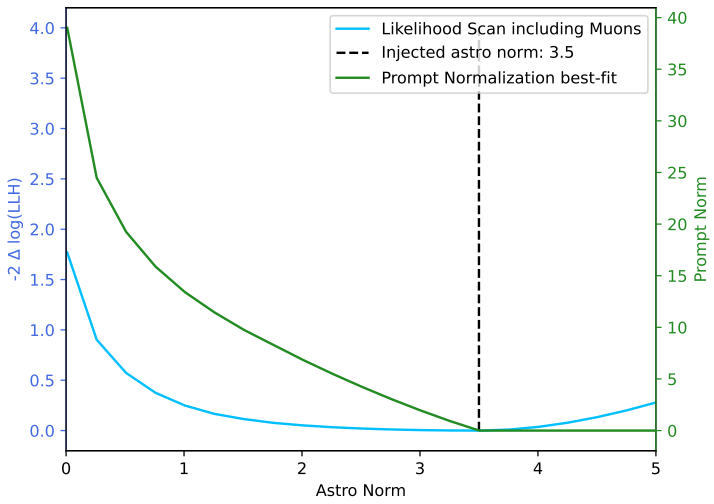

Figure 5.6: Asimov Poisson likelihood scan, for ARCA21, 287 days, including atmospheric muons, and fitting the prompt and conventional norm separately. The injected flux parameters are $\Phi_{\text{astro}} = 3.5$, $\gamma_{\text{astro}} = 3.3$, $\Phi_{\text{muons}} = 1.0$, and $\Phi_{\text{conv+prompt}} = 1.0$. The green line shows the best-fit values of the prompt normalization in each scan point.

varied datasets: 90%, and 110% quantum efficiency of the standard MC implementation. The gradient for each bin is calculated as shown in the example Figure A.2 for the absorption length and Figure A.3 for the quantum efficiency for a specific binning. With that, the systematic parameters can be obtained within the fitting process. The functionality of the detector systematics is checked by two-dimensional Asimov likelihood scans on the signal parameters: astrophysical normalization and spectral index.

It is expected that by introducing the systematic parameters *abs* for absorption length and QE for quantum efficiency into the Asimov fit, the sensitivity to the signal parameters decreases. Introducing more fit parameters results in more degrees of freedom for the fit, and the variance during the fit process increases. This is tested by performing the likelihood scan with and without systematic parameters (c.f. Figure 5.8). Both scans are performed with a zenith binning of 6 zenith bins and include the atmospheric muon model. The systematic parameters in the Asimov dataset are set to $abs = 0$ and $QE = 0$. This represents no change in the systematics from the original MC dataset. For the systematic parameters, some Gaussian priors are set in the Fit. The Gaussian mean μ of the systematic parameters is set to $\mu = 0$, the Gaussian variance σ^2 is set to $\sigma^2 = 2$, and the bounds $[a, b]$ of the Gaussian functions are set to $[0, 10]$.

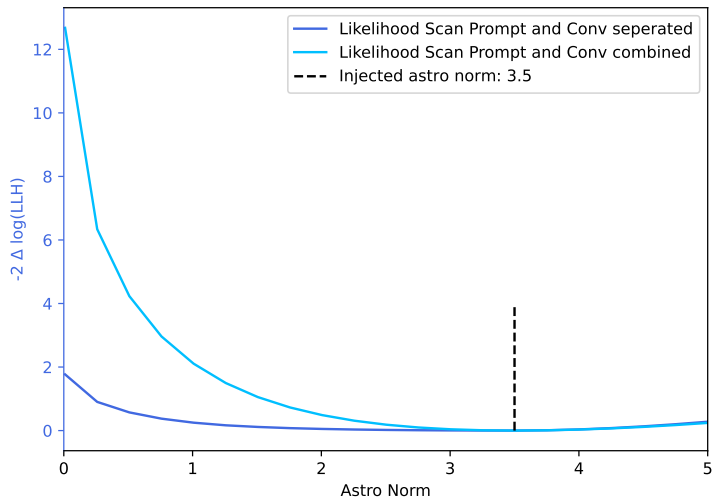

Figure 5.7: Asimov Poisson likelihood scan, for ARCA21, 287 days, comparing the likelihood scans, fitting the prompt and conventional combined or separately. The injected flux parameters are $\Phi_{\text{astro}} = 3.5$, $\gamma_{\text{astro}} = 3.3$, $\Phi_{\text{muons}} = 1.0$, and $\Phi_{\text{conv+prompt}} = 1.0$.

The likelihood scans in Figure 5.8 show that the implementation of systematic parameters works as expected. The contour on the signal parameters without systematic parameters added to the fit is closed up to the 99% confidence contour. In comparison to that, the 2σ contour in the likelihood scan, including *abs* and QE systematic parameters, is not closed. This means higher uncertainties on the best-fit of the astrophysical normalization when detector systematics are included.

5.6 Snakemake Workflow for ARCA21 All-Sky Diffuse Analysis

All of the analysis steps described in the previous sections are included in one Snakemake workflow. The data analysis is handled, starting from the DST files to obtaining a plot with the likelihood scan. A schematic of the workflow is shown in Figure 5.9. The entire analysis process can be managed with just two configuration files. The snakemake-config file handles the input files needed for the workflow, the event selection used, and the likelihood scans performed. The other configuration file, pyFF-config, handles the analysis parameters required by pyFF. This file defines the models used for the analysis, the injected parameters for Asimov tests, the analysis binning, and the priors used to fit parameters.

The KM3NeT collaboration saves reconstructed atmospheric muon and neutrino Monte Carlo (MC) simulations in DST files in the .root format. All the analysis-relevant

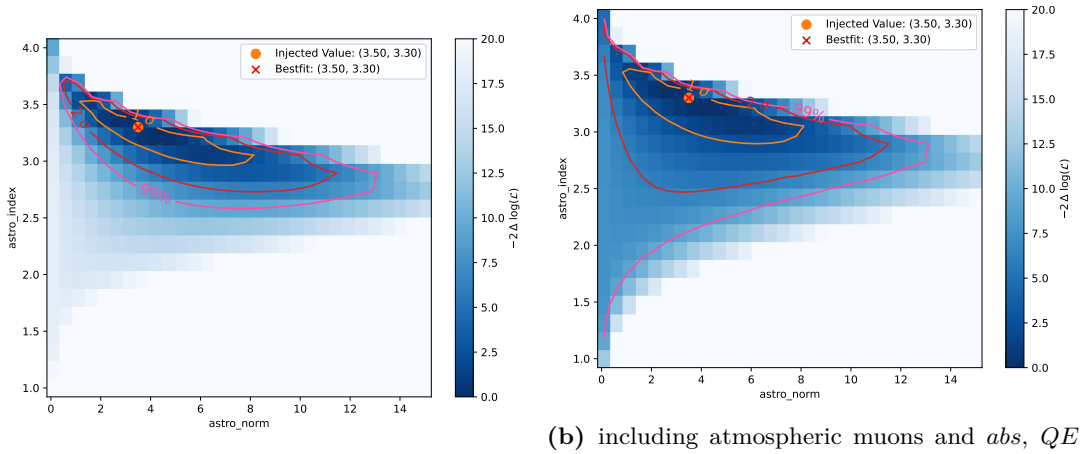

(a) including atmospheric muons, no systematics

(b) including atmospheric muons and *abs*, *QE* systematics

Figure 5.8: Poisson likelihood contours for Asimov all-sky diffuse analysis. In plot (a), the atmospheric muon model is included, and no detector systematics. In plot (b), the detector systematic parameters *abs*, and *QE* are added in the fit. For both fits, a zenith binning of 6 zenith bins is used. The confidence contours are shown for the 1σ (orange), the 2σ (red), and the 99% (pink) confidence contour.

variables are then retrieved and saved into a pandas data frame. The first cuts, including the pre- and first-level cuts, can then be applied. For neutrino weighting, MCEq splines are created. These splines and the neutrino data frames are then used in the atmospheric flux weighting step. Additionally, the baseline weights needed for pyFF are calculated. The only difference in the last step is the process for the atmospheric muon events. In order to scale the atmospheric muons in the analysis by an arbitrary livetime, the baseline weights also have to be calculated: $w_{\text{baseline}}^{\text{muons}} = w_{\text{muon}} \cdot t_{\text{DAQ-livetime}}/t_{\text{livetime}}/n_{\text{tot}}$.

Additionally, the BDT cut optimization can be included in the Snakemake workflow to obtain the sensitivity-optimized BDT cut value. This value can then be used as an input parameter for the final event selection. The final event selection is applied when creating the dictionary needed as input for PyFF. This data frame contains only the variables required for the likelihood scan.

To perform likelihood scans including systematic parameters, the gradients from the varied systematic datasets are also needed. The systematic datasets are processed through a similar chain as the neutrino MC files, but without BDT optimization. The event selection of the baseline dataset is automatically also applied to the systematic datasets. The analysis histograms are created from the weighted systematic datasets, and the gradient fits are performed. These gradient fits are saved and used as input

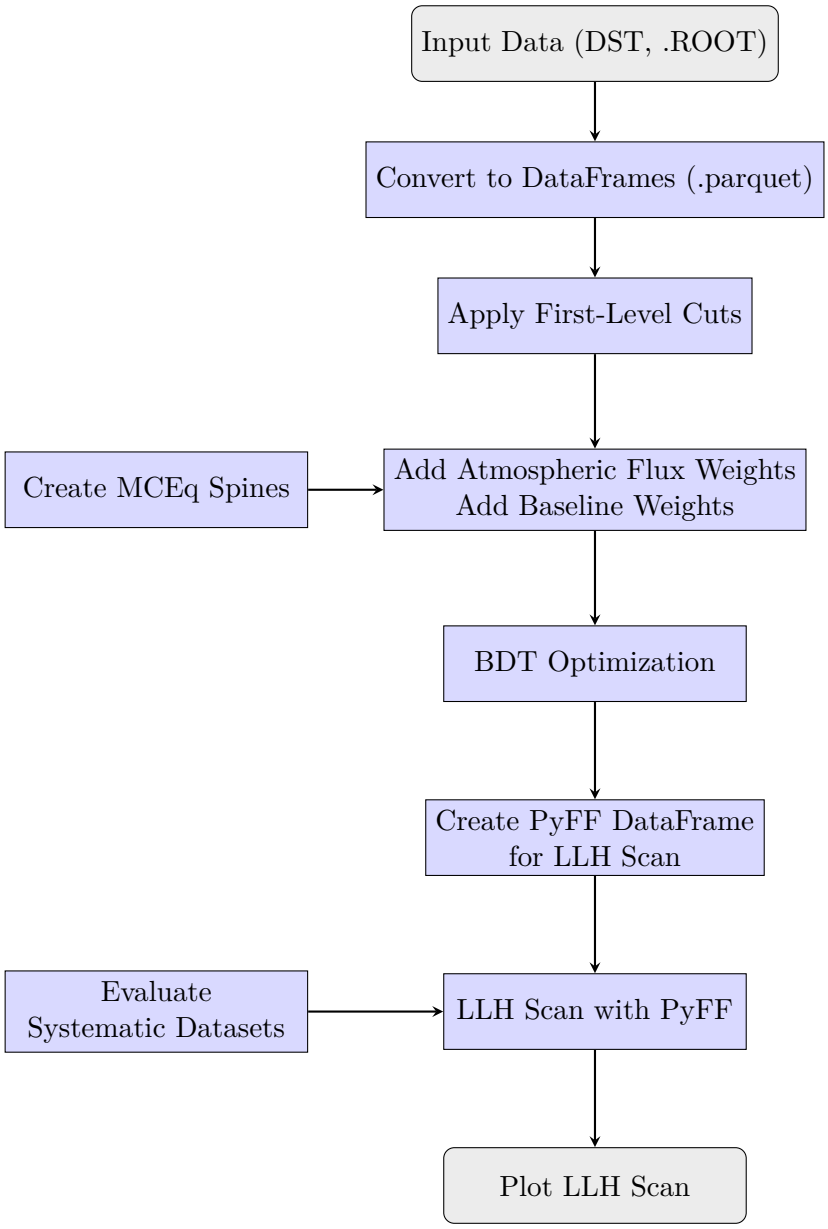

Figure 5.9: Schematic overview of the Snakemake workflow used in the ARCA21 all-sky diffuse analysis. The pipeline converts input DST data into usable dataframes, applies initial cuts, includes MCEq spines and atmospheric flux weights, performs BDT optimization, constructs the PyFF dataframe for the likelihood evaluation, incorporates systematic variations, runs the LLH scan, and finally produces the resulting plots.

for the likelihood scans. For each different choice of binning and input parameters in the PyFF config, the gradients are recalculated.

These inputs allow for likelihood scans using pyFF, where the scanned regions are determined by the snakemake config. The results of the likelihood scans are input into the plotting script, which produces scans including likelihood contours.

The advantage of this workflow is that it makes the entire analysis chain traceable and reproducible. Additionally, steering is made convenient, as only two configuration files are needed for the full analysis. This analysis chain can easily be adapted for use in other analyses. It can be used either in combination with different ARCA configurations or for analyses on the galactic plane.

5.7 Comparison to KM3NeT All-Sky Diffuse Analyes

After implementing all necessary systematics, a comparison to an already existing frequentist measurement of the all-sky diffuse flux from the KM3NeT Collaboration using the same data sample is performed [48]. This analysis is currently performed on MC simulations only. Their current injected values on the signal parameters are the published IceCube results for the 9.5 years of IceCube analysis. The IceCube Collaboration's best-fit values in this analysis on the diffuse astrophysical flux are $\Phi_{\text{astro}} = 1.44$, and $\gamma_{\text{astro}} = 2.37$ [4]. The results for an Asimov fit obtained for ARCA21 by the frequentist approach are shown in Figure 5.10. It shows the 99% confidence contour, scanning the astrophysical normalization and the spectral index, for injecting the IceCube best-fit values. The systematic handling differs from the approach used in pyFF. Within that analysis, three sources of systematic uncertainties are implemented. The atmospheric muon uncertainty is set to 40% and accounted for in every analysis bin. Also, for the atmospheric neutrinos, an uncertainty of 45% is accounted for in every bin. For the cosmic neutrinos, an uncertainty of 20% is assumed, which scales as a normalization parameter over all bins. The analysis uses an energy binning of 12 bins in the energy range $10^3\,\text{GeV} < E_\nu < 10^6\,\text{GeV}$.

The same binning and energy range is used in the pyFF analysis, as shown in Figure 5.11. The 99% confidence contour is shown in pink. On the axis of the astrophysical normalization, the contour reaches a maximal astrophysical normalization of $\Phi_{\text{astro}} \approx 12.4$. In comparison to that, the KM3NeT frequentist analysis shows a 99% confidence contour on the astrophysical normalization to $\Phi_{\text{astro}} \approx 11.5$. That means the pyFF analysis with the same binning is less sensitive to the astrophysical neutrino flux. Neither 99% confidence likelihood contour is closed. A closed contour would correlate to exclude the background hypothesis of no astrophysical neutrino flux with that significance. In the pyFF likelihood scan is also shown that with the injected parameters, the 1σ likelihood contour is not closed. One difference in the likelihood contours is

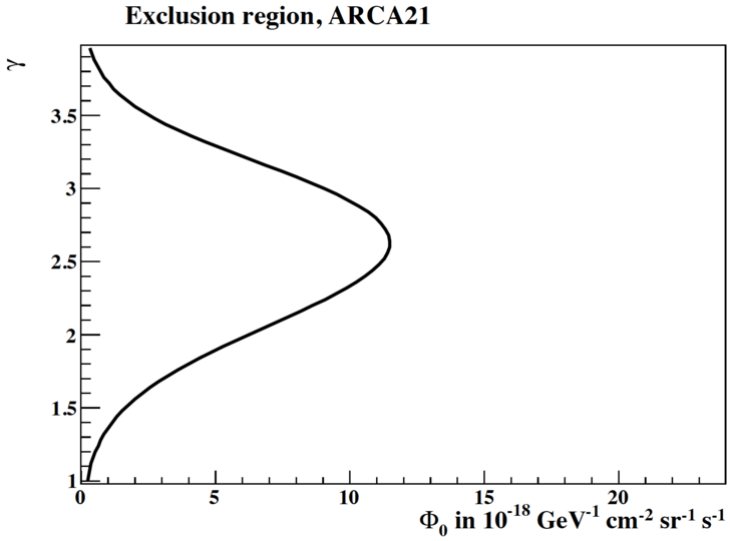

Figure 5.10: Two-dimensional Asimov likelihood scan for ARCA21 on the astrophysical normalization on the x-axis and the spectral index on the y-axis. The injected signal parameters on the Asmimov dataset are $\Phi_{\text{astro}} = 1.44$, and $\gamma_{\text{astro}} = 2.37$. The likelihood contour of the 99% confidence interval is shown. The plot is taken from [48].

that the pyFF contour is asymmetric on the spectral index axis, whereas the KM3NeT frequentist shows a symmetric likelihood contour. The asymmetric shape is expected, as a higher spectral index implies more high-energy astrophysical neutrinos in the signal region. With that, it is more sensitive to the astrophysical neutrino flux.

For ARCA21, there is already an all-sky diffuse unblinded, which uses a Bayesian approach. The likelihood scan performed on the data is shown in Figure 5.13 [43]. The best-fit parameters obtained in that analysis on the signal parameters are $\Phi_{\text{astro}} = 3.5$, and $\gamma_{\text{astro}} = 3.3$. The 68% confidence contour is almost closed. In the Bayesian analysis, uncertainties are accounted for in the water absorption length, the PMT quantum efficiency, and the atmospheric neutrino flux. For all three of these systematic parameters, a total uncertainty of 45% is estimated from the MC samples with varied systematics for ARCA21 [43].

This analysis uses, as the frequentist analysis, only a binning on the energy axis. The energy ranges from $10^4\,\text{GeV} < E_\nu < 10^6\,\text{GeV}$, and 8 bins are used. The same binning and energy range is used for the likelihood scan shown in Figure 5.13. The likelihood scan in PyFF also indicates less confidence in the astrophysical neutrino flux than the KM3NeT analysis. The 1σ contour is for no spectral index values closed on the normalization axis. The differences can be explained by the different approaches to systematic uncertainty modelling.

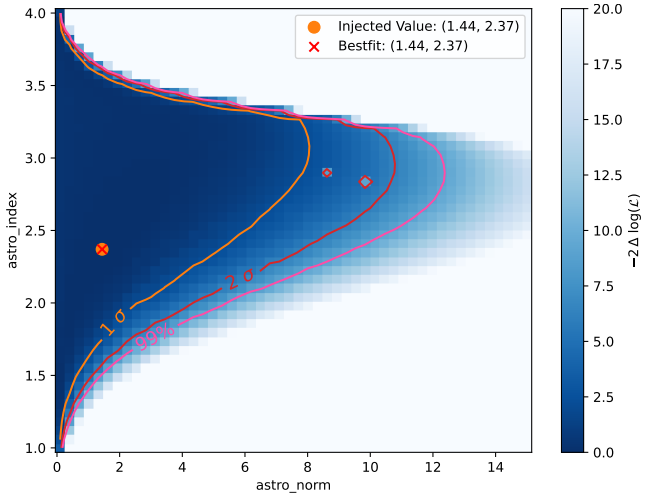

Figure 5.11: Two-dimensional Poisson Asimov likelihood scan for ARCA21 on the astrophysical normalization with injected signal parameters $\Phi_{\text{astro}} = 1.44$, and $\gamma_{\text{astro}} = 2.37$. The likelihood scan shows the 1σ, 2σ, and 99% confidence intervals on the two signal parameters. The injected value and best-fitted value are the same, as a Poisson likelihood is used. The two small red circles mark failed likelihood scans in single scan points.

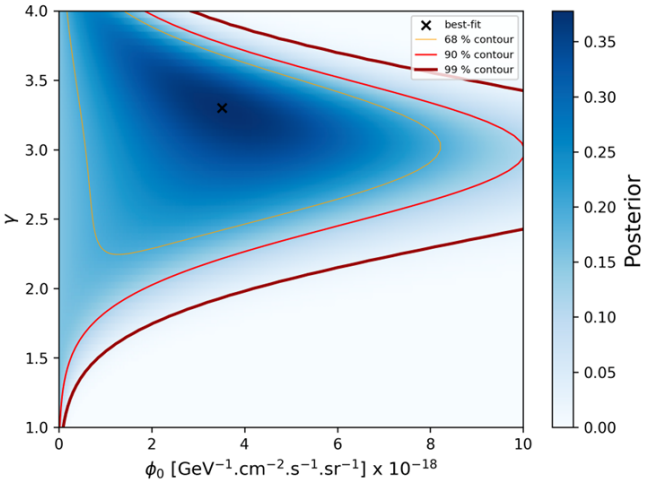

Figure 5.12: Two-dimensional likelihood scan for ARCA21 on the astrophysical normalization on the x-axis and the spectral index on the y-axis. This plot is created by Vasileios Tsourapis with his unblinded Bayesian all-sky diffuse analysis, fitting on data. The best-fit parameters obtained in the bis on the signal parameters are $\Phi_{\text{astro}} = 3.5$, and $\gamma_{\text{astro}} = 3.3$. The likelihood scan shows the 68%,90%, and 99% confidence intervals on the two signal parameters.

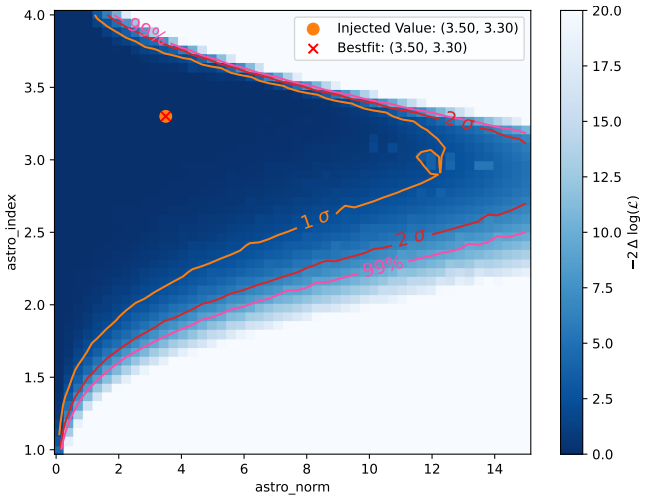

Figure 5.13: Two-dimensional Poisson Asimov likelihood scan for ARCA21 on the astrophysical normalization with injected signal parameters $\Phi_{\text{astro}} = 3.5$, and $\gamma_{\text{astro}} = 3.3$. The likelihood scan shows the 1σ, 2σ, and 99% confidence intervals on the two signal parameters. The injected value and best-fitted value are the same, as a Poisson likelihood is used. The lopp in the 1σ contour marks failed likelihood scans in the scan points.

In contrast to the KM3NeT analysis, the pyFF analysis could improve in sensitivity by adding zenith binning. Figure 5.14 ashows several likelihood scans performed on the Asimov dataset using the Poisson likelihood with different numbers of zenith bins. The same values used in the KM3NeT frequentist analysis are injected in these fits. This demonstrates that sensitivity to the astrophysical normalisation increases with the introduction of zenith bins. All the likelihood contours shown are smaller on that axis than in Figure 5.11, where no zenith bins are used. However, adding more than three zenith bins does not significantly improve the sensitivity. The reason for the increasing significance of adding zenith bins in the pyFF analysis could be the different systematic handling than in the KM3NeT frequentis analysis. In the pyFF analysis, only two new fit parameters are introduced for the detector systematics and two additional fit parameters for the uncertainties on the atmospheric flux. In contrast, the KM3NeT frequentist analysis adds uncertainty parameters to each analysis bin. In that case, by increasing the bin numbers, the number of fit parameters also increases. This leads to more degrees of freedom and larger uncertainties in the fit. So the optimal number of zenith bins has to be tested in further analyses.

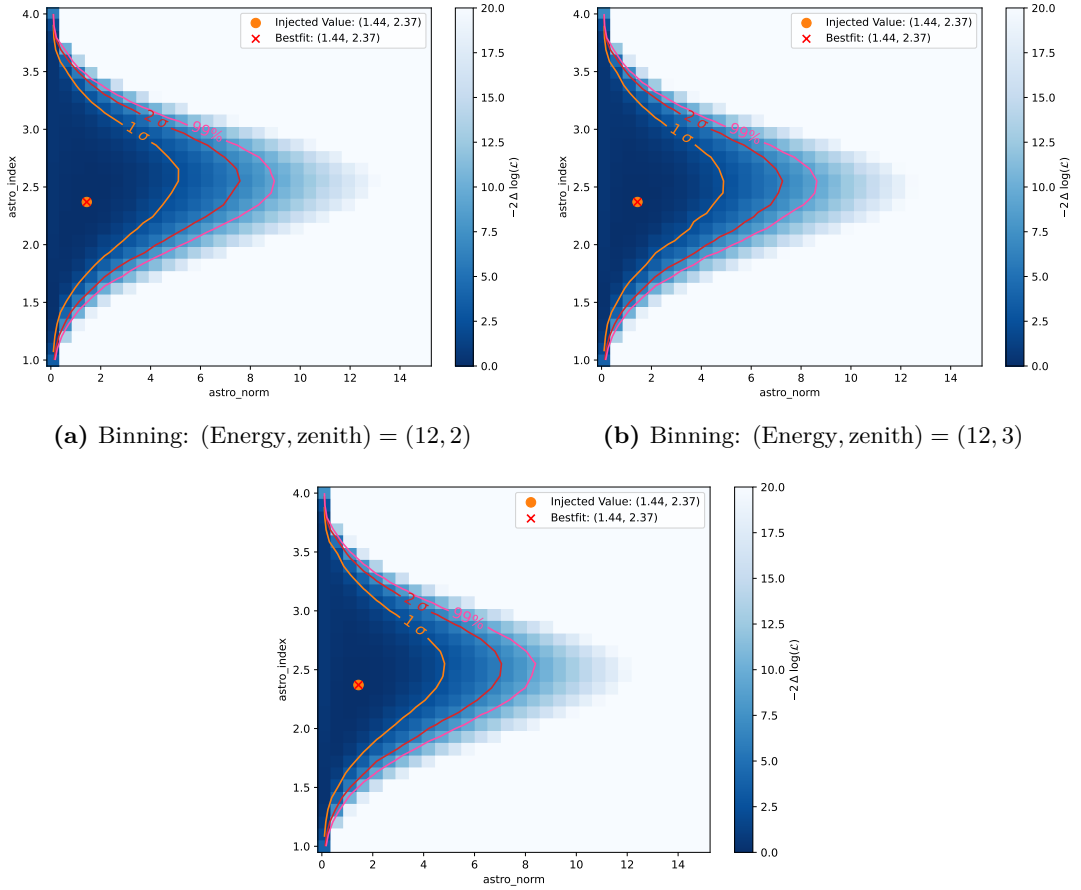

(a) Binning: (Energy, zenith) = (12, 2)

(b) Binning: (Energy, zenith) = (12, 3)

(c) Binning: (Energy, zenith) = (12, 9)

Figure 5.14: Likelihood contours for Poisson Asimov all-sky diffuse analysis, including atmospheric muons and systematic uncertainties, using different numbers of zenith bins. The scanned parameters are the signal parameters, astrophysical normalization, and spectral index. The injected free parameters are: $\Phi_{\text{astro}} = 1.44$, $\gamma_{\text{astro}} = 2.37$, $\Phi_{\text{conv}} = 1.0$, $\Phi_{\text{prompt}} = 0.0$, $\Phi_{\text{muons}} = 1.0$, $abs = 0$, $QE = 0$. The confidence contours are shown for the 1σ (orange), the 2σ (red), and the 99% (pink) confidence contour.

6 Conclusion

This thesis focuses on the first steps towards a joint IceCube-KM3NeT galactic analysis. In chapter 4, sensitivity studies on the galactic plane are performed. These tests aim to demonstrate how combining data from two neutrino telescopes improves a galactic plane analysis of track events only. To achieve this, data from the IceCube detector at the South Pole and the ARCA detector in the Mediterranean Sea are used. The location of the detectors is of major importance for analysing track events on the galactic plane. IceCube is only sensitive to the part of the galactic plane located in the northern sky, whereas ARCA is sensitive to 90% of the galactic plane, including the galactic centre.

The ARCA detector is currently under construction, and the latest data-taking period used the ARCA21 configuration, which had a live time of 287 days. For IceCube, a live time of 11.67 days can be accounted for. This thesis demonstrates that adding the ARCA21 MC dataset to the IceCube MC dataset has a negligible impact on the joint fit sensitivity on the galactic plane. However, as ARCA is still under construction, the first MC datasets were simulated for the ARCA115 detector configuration by KM3NeT. Assuming the ARCA115 detector is built in 2028, the sensitivity on the galactic plane for ARCA115 will be the same as that of the IceCube detector, after five years of operation.

To enhance collaboration and modernize the software, the open-source program PyFF will be used for further joint analyses. To verify the framework's functionality, an all-sky diffuse analysis for ARCA21 has been set up (c.f. chapter 5). Within that, methods for handling the atmospheric muon background and systematic errors for the ARCA21 detector are also employed. Within the diffuse all-sky analysis, the atmospheric muon background can be accounted for by adding the simulated muons to the analysis histogram. This makes it possible to optimise the event selection by choosing a BDT cut for the sensitivity of the analysis. Systematic uncertainties can now be added to the ARCA21 analysis. This is achieved by using various systematic MC datasets. A gradient is obtained from these, which can be fitted to the analysis histogram. The whole analysis chain is implemented into one Snakemake workflow. This allows easy handling of changing the analysis configurations and ensures reproducibility. This analysis demonstrates the agreement between the pyFF framework and the KM3NeT frequentist analysis.

Once the principle of the ARCA21 diffuse all-sky analysis has been verified, it can be improved and optimised to increase sensitivity. One possible improvement is to refine the handling of the atmospheric muon background. It is useful to model a smooth muon distribution within the analysis binning. For this purpose, a kernel density estimate (KDE) can be used, which can be constructed using normalised flows. Another improvement could be made in the handling of the detector systematics. Currently, the detector systematic handling has the issue that a certain neutrino flux must be injected to obtain the required gradients for the analysis fit. This can be overcome by using hypersurfaces that interpolate between varied systematic datasets. To improve sensitivity in the likelihood scan, the analysis binning can be optimised. For comparisons with KM3NeT results, only energy binning is used. However, zenith binning could also enhance the sensitivity of the analysis. This would need to be tested with respect to the MC statistics per bin. To verify the choice of binning, fits can be performed on small data samples to check the agreement between the data and the MC. Additionally, the sensitivity of the analysis to the astrophysical neutrino flux can be enhanced by including future and past ARCA configurations. The Snakemake pipeline makes it feasible to process the MC of various detector configurations. In pyFF, joint fits across different configurations of the same detector or entirely different detectors can also be performed.

With these improved analysis methods, the next goal is to unblind the analysis. This will demonstrate the sensitivity of the pyFF analysis method to data. It can then be compared to the best-fit results obtained by the unblinded all-sky diffuse analysis. This final verification step would open up the use of the pyFF framework for galactic analyses. The next step is therefore to implement a joint analysis for IceCube and ARCA, including background and systematic handling. Such analyses can be verified with the ARCA21 version. However, joint analyses will become increasingly important for future detector configurations. Compared to the ARCA21 configuration analyzed within this thesis, the volume of the current ARCA51 detector has already more than doubled. In addition to the full ARCA230 detector, plans are in place for the IceCube-Gen2 detector. This detector is planned to be an $8\,\mathrm{km}^3$ array in the Antarctic ice [51]. Combining the full ARCA and the IceCube-Gen2 detectors could open up new fields of neutrino astronomy.

Bibliography

[1] European Space Agency (ESA) Science Technology. *A history of astrometry – Part I: Mapping the sky from ancient to pre-modern times*. https://sci.esa.int/web/gaia/-/53196-the-oldest-sky-maps. [Online; accessed 04-December-2025]. 2019.

[2] IceCube Collaboration. 'Evidence for High-Energy Extraterrestrial Neutrinos at the IceCube Detector'. In: *Science* 342.6161 (Nov. 2013). ISSN: 1095-9203. DOI: 10.1126/science.1242856. URL: http://dx.doi.org/10.1126/science.1242856.

[3] IceCube Collaboration. 'Observation of high-energy neutrinos from the Galactic plane'. In: *Science* 380.6652 (June 2023), pp. 1338–1343. ISSN: 1095-9203. DOI: 10.1126/science.adc9818. URL: http://dx.doi.org/10.1126/science.adc9818.

[4] IceCube Collaboration. *Neutrino History*. https://icecube.wisc.edu/category/neutrino-history/. [Online; accessed 03-October-2025].

[5] Thomas K. Gaisser, Ralph Engel and Elisa Resconi. 'Cosmic Rays and Particle Physics'. In: Cambridge University Press, 2016.

[6] KATRIN. 'Direct neutrino-mass measurement based on 259 days of KATRIN data'. In: *Science* 388.6743 (Apr. 2025), pp. 180–185. ISSN: 1095-9203. DOI: 10.1126/science.adq9592. URL: http://dx.doi.org/10.1126/science.adq9592.

[7] Roberto Aloisio, Eugenio Coccia and Francesco Vissani, eds. *Multiple Messengers and Challenges in Astroparticle Physics*. Cham: Springer International Publishing, 2018. ISBN: 978-3-319-65423-2. DOI: 10.1007/978-3-319-65425-6.

[8] Jaime Alvarez-Muniz et al. 'Cosmic Rays'. In: *Review of Particle Physics (Particle Data Group)* (2024). Revised March 2024. URL: https://pdg.lbl.gov/2024/reviews/rpp2024-rev-cosmic-rays.pdf.

[9] James J. Beatty, James Matthews and Scott P. Wakely. 'Cosmic Rays'. In: *Review of Particle Physics (Particle Data Group)* (2022). Revision October 2021. URL: https://pdg.lbl.gov/2022/reviews/rpp2022-rev-cosmic-rays.pdf.

[10] Matthew G. Baring. 'Diffusive shock acceleration: The Fermi mechanism'. In: *32nd Rencontres de Moriond: High-Energy Phenomena in Astrophysics*. 1997, pp. 97–106. arXiv: astro-ph/9711177.

[11] Thomas K. Gaisser and M. Honda. 'Flux of Atmospheric Neutrinos'. In: *Annual Review of Nuclear and Particle Science* 52 (2002), pp. 153–199. DOI: 10.1146/annurev.nucl.52.050102.090645.

[12] For the IceCube Collaboration: Boettcher Jakob. 'Search for the Prompt Atmospheric Neutrino Flux in IceCube'. In: *PoS* ICRC2023 (2023). DOI: 10.22323/1.444.1068.

[13] IceCube Collaboration. 'Improved Characterization of the Astrophysical Muon–neutrino Flux with 9.5 Years of IceCube Data'. In: *The Astrophysical Journal* 928.1 (Mar. 2022), p. 50. ISSN: 1538-4357. DOI: 10.3847/1538-4357/ac4d29. URL: http://dx.doi.org/10.3847/1538-4357/ac4d29.

[14] Tommaso Montaruli. *Lecture 10: The Cherenkov Effect and Related Topics*. https://user-web.icecube.wisc.edu/~tmontaruli/801/lect10.pdf. [Online; accessed 03-October-2025].

[15] IceCube Collaboration. *IceCube: Detector*. https://icecube.wisc.edu/science/icecube/. [Online; accessed 20-November-2025]. 2025.

[16] Leif Rädel and Christopher Wiebusch. 'Calculation of the Cherenkov light yield from electromagnetic cascades in ice with Geant4'. In: *Astroparticle Physics* 44 (2013). DOI: 10.1016/j.astropartphys.2013.02.006. URL: https://www.sciencedirect.com/science/article/abs/pii/S092765051300025X.

[17] KM3NeT Collaboration. 'Letter of intent for KM3NeT 2.0'. In: *Journal of Physics G: Nuclear and Particle Physics* 43.8 (June 2016), p. 084001. ISSN: 1361-6471. DOI: 10.1088/0954-3899/43/8/084001. URL: http://dx.doi.org/10.1088/0954-3899/43/8/084001.

[18] KM3NeT Collaboration. *The neutrino detectors*. https://www.km3net.org/research/detector/. [Online; accessed 04-October-2025].

[19] IceCube Collaboration. *Improved measurements of the TeV–PeV extragalactic neutrino spectrum from joint analyses of IceCube tracks and cascades*. 2025. arXiv: 2507.22234 [astro-ph.HE]. URL: https://arxiv.org/abs/2507.22234.

[20] IceCube Collaboration. 'Energy reconstruction methods in the IceCube neutrino telescope'. In: *Journal of Instrumentation* (2014). DOI: 10.1088/1748-0221/9/03/P03009.

[21] IceCube Collaboration. 'All-sky Neutrino Point-source Search with IceCube Combined Track and Cascade Data'. In: *The Astrophysical Journal* (Dec. 2025), p. 11. DOI: 10.3847/1538-4357/ae113f. URL: https://doi.org/10.3847/1538-4357/ae113f.

[22] Christian Haack. *NNMFit*. Version 0.4.0. 2023. URL: https://github.com/icecube/NNMFit.

[23] PLEnuM-group. *pyForwardFolding*. https://github.com/PLEnuM-group/pyForwardFolding/tree/main. 2025.

[24] Tetiana Kozynets, Anatoli Fedynitch and D. Jason Koskinen. 'Atmospheric lepton fluxes via two-dimensional matrix cascade equations'. In: *Phys. Rev. D* 108 (10 Nov. 2023), p. 103040. DOI: 10.1103/PhysRevD.108.103040. URL: https://link.aps.org/doi/10.1103/PhysRevD.108.103040.

[25] Georg Schwefer, Philipp Mertsch and Christopher Wiebusch. 'Diffuse Emission of Galactic High-energy Neutrinos from a Global Fit of Cosmic Rays'. In: *The Astrophysical Journal* 949.1 (May 2023), p. 16. ISSN: 1538-4357. DOI: 10.3847/1538-4357/acc1e2. URL: http://dx.doi.org/10.3847/1538-4357/acc1e2.

[26] Carla Distefano. *Event weights in KM3NeT simulations*. GitHub Pages, Gitrelease: cad5c91,date2022-02-17T04:24:42+0100. February 17, 2022. URL: https://git.km3net.de/simulation/documents/event-weighting_documentation (visited on 12/08/2025).

[27] KM3NeT Collaboration. 'gSeaGen: The KM3NeT GENIE-based code for neutrino telescopes'. In: *Computer Physics Communications* 256 (Nov. 2020), p. 107477. ISSN: 0010-4655. DOI: 10.1016/j.cpc.2020.107477. URL: http://dx.doi.org/10.1016/j.cpc.2020.107477.

[28] KM3NeT-Collaboration. 'gSeaGen: The KM3NeT GENIE-based code for neutrino telescopes'. In: *Computer Physics Communications* 256 (Nov. 2020), p. 107477. ISSN: 0010-4655. DOI: 10.1016/j.cpc.2020.107477. URL: http://dx.doi.org/10.1016/j.cpc.2020.107477.

[29] KM3NeT Collaboration. *JPP*. https://git.km3net.de/common/jpp. internal only. 2025.

[30] KM3NeT Wiki. *Glossary*. [Online; accessed 12-December-2025], internal only. 2025. URL: https://wiki.km3net.de/index.php/Glossary.

[31] KM3NeT Wiki. *Data Processing and Data Quality (DPDQ)*. [Online; accessed 11-August-2025], internal only. 2025. URL: https://wiki.km3net.de/index.php/Data_Processing_and_Data_Quality_(DPDQ).

[32] Askhat Gazizov and Marek Kowalski. 'ANIS: High energy neutrino generator for neutrino telescopes'. In: *Computer Physics Communications* 172.3 (2005), pp. 203–213. DOI: 10.1016/j.cpc.2005.03.235.

[33] Christian Haack. *NNMFit's documentation*. URL: https://user-web.icecube.wisc.edu/~rnaab/GlobalFit/NNMFit/docs_beta/.

[34] Carlos A. Argüelles, A. Schneider and Tracy Yuan. 'A binned likelihood for stochastic models'. In: *Journal of High Energy Physics* (June 2019), p. 030. ISSN: 1029-8479. DOI: 10.1007/JHEP06(2019)030. URL: https://doi.org/10.1007/JHEP06(2019)030.

[35] Glen Cowan. *Statistical Data Analysis*. Oxford; New York: Oxford University Press, 1998. ISBN: 978-0-19-850155-8.

[36] Glen Cowan et al. 'Asymptotic formulae for likelihood-based tests of new physics (vol 71, pg 1554, 2011)'. In: *European Physical Journal C* (July 2013). DOI: 10.1140/epjc/s10052-013-2501-z.

[37] Samuel S. Wilks. 'The Large-Sample Distribution of the Likelihood Ratio for Testing Composite Hypotheses'. In: *Annals of Mathematical Statistics* 9.1 (1938), pp. 60–62. DOI: 10.1214/aoms/1177732360.

[38] Brandon T. Willard et al. *Aesara*. https://github.com/aesara-devs/aesara. 2023.

[39] For the IceCube collaboration Fuerst Philipp Michael. 'Galactic and Extragalactic Analysis of the Astrophysical Muon Neutrino Flux with 12.3 years of IceCube Track Data'. In: *PoS* ICRC2023 (2023). DOI: 10.22323/1.444.1046.

[40] Roy Frostig et al. *JAX: Composable transformations of Python+NumPy programs*. https://github.com/google/jax. 2024.

[41] Leif Rädel. 'Measurement of High-Energy Muon Neutrinos with the IceCube Neutrino Observatory'. Dissertation, RWTH Aachen University; Online unter https://publications.rwth-aachen.de/record/709576. PhD thesis. Aachen: RWTH Aachen University, 2017. DOI: 10.18154/RWTH-2017-10054.

[42] IceCube Collaboration. 'Evidence for neutrino emission from the nearby active galaxy NGC 1068'. In: *Science* 378.6619 (Nov. 2022), pp. 538–543. ISSN: 1095-9203. DOI: 10.1126/science.abg3395. URL: http://dx.doi.org/10.1126/science.abg3395.

[43] KM3NeT Wiki. *Diffuse analysis + Galactic ridge ARCA6 — KM3NeT Wiki*. [Online; accessed 10-November-2025], internal only. 2025. URL: https://wiki.km3net.de/index.php?title=Diffuse_analysis_%2B_Galactic_ridge_ARA6&oldid=43768.

[44] Nadja Lessing. *ARCA115 sensitivity to quantum decoherence*. internal technical note. 2025. URL: https://drive.google.com/file/d/1QlZX_ksjRYsMtreothUgL_TFv0GbwYp/view.

[45] NASA. *Basics of Space Flight – Chapter 2: Reference Systems*. [Online; accessed 12-October-2025]. National Aeronautics and Space Administration. 2024. URL: https://science.nasa.gov/learn/basics-of-space-flight/chapter2-2/.

[46] For the IceCube Collaboration: Janik Oliver. 'Using End-to-End Optimized Summary Statistics to Improve IceCube's Diffuse Galactic Fits'. In: *PoS* ICRC2025 (2025). DOI: 10.22323/1.501.1132.

[47] Vasileios Tsourapis et al. 'All-sky diffuse astrophysical neutrino flux with KM3NeT/ARCA data'. In: *PoS* ICRC2025 (2025). DOI: 10.22323/1.501.1196.

[48] KM3NeT Wiki. *Frequentist analysis of the all-sky diffuse flux — KM3NeT Wiki*. [Online; accessed 17-November-2025], internal only. 2025. URL: https:

//wiki.km3net.de/index.php?title=Frequentist_analysis_of_the_all-sky_diffuse_flux&oldid=44211.

[49] Johannes Köster and Contributors. *Snakemake Documentation*. https://snakemake.readthedocs.io/en/stable/. [Online; accessed 13-November-2025]. 2025.

[50] Jakob Böttcher. 'Exploring Atmospheric Neutrino Fluxes: Seasonal Variations and Prompt Neutrino Search in the IceCube Neutrino Observatory'. Dissertation. RWTH Aachen University, Mar. 2025.

[51] IceCube-Gen2 Collaboration. 'IceCube-Gen2: the window to the extreme Universe'. In: *Journal of Physics G: Nuclear and Particle Physics* 48.6 (Apr. 2021), p. 060501. ISSN: 1361-6471. DOI: 10.1088/1361-6471/abbd48. URL: http://dx.doi.org/10.1088/1361-6471/abbd48.

A Appendix - All-Sky Diffuse Analysis

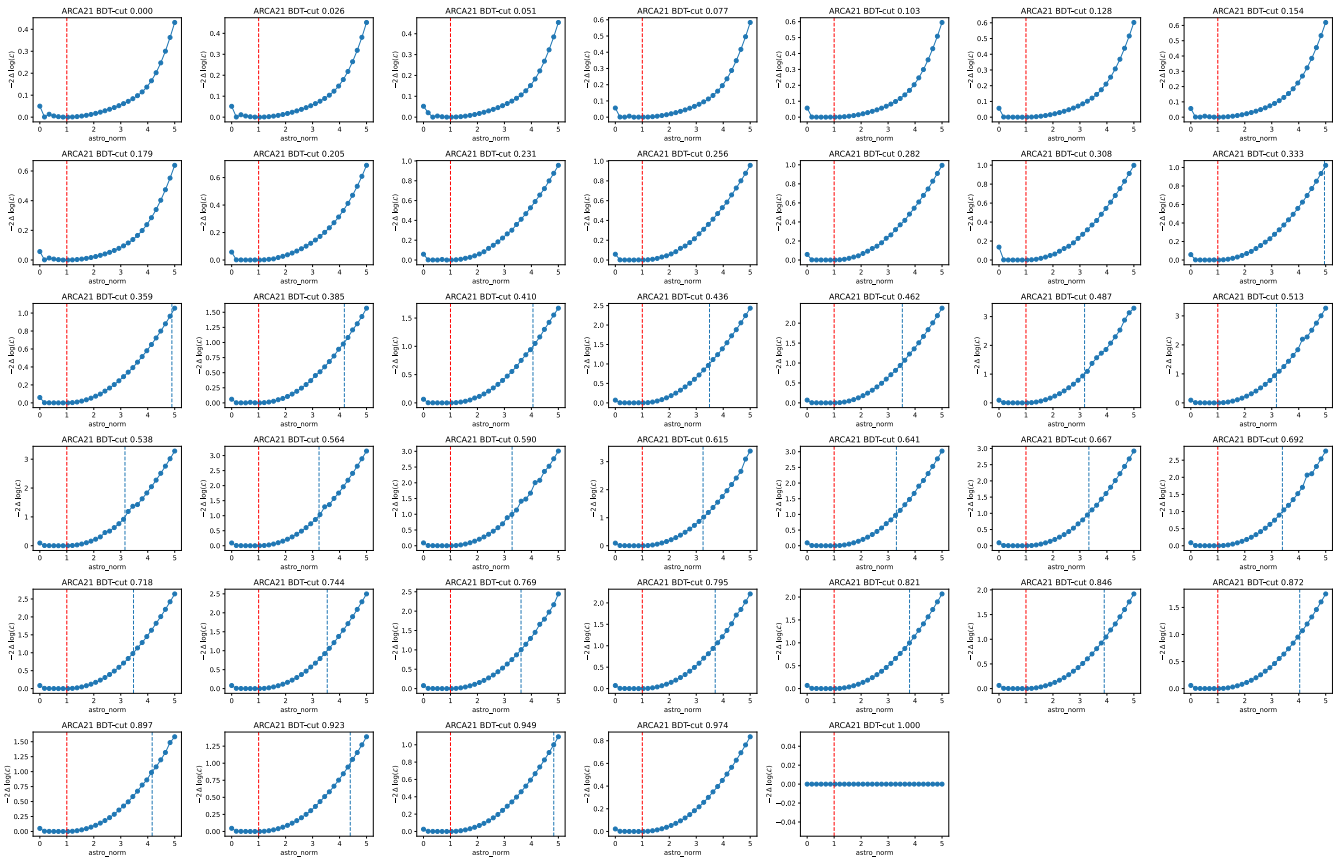

Figure A.1: Poisson Asimov likelihood scans, for different BDT cuts between $BDT = 0$ and $BDT = 1$. The scanned parameter is the normalization of the astrophysical neutrino flux. The injected values in the Asimov dataset are $\Phi_{\text{astro}} = 1$ (indicated as the red dashed line), and $\gamma_{\text{astro}} = 2.37$ on the signal parameters. The blue dashed line marks the limits of the 1σ confidence interval. This is not contained in the scanned area of all likelihood scans. Important to note is that the muon weighting within these likelihood scans is not correctly implemented, and the prompt and conventional norms are fitted separately.

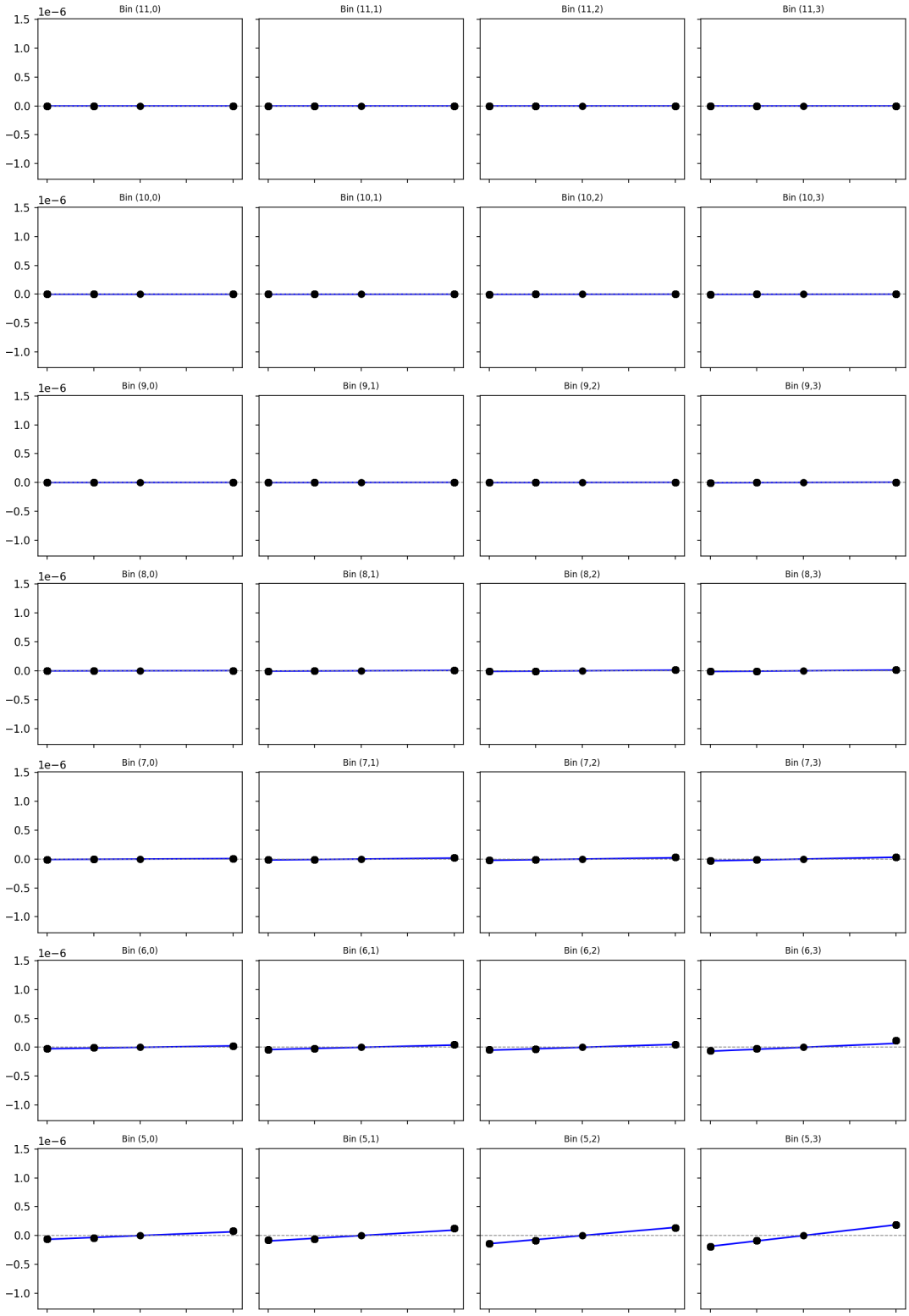
Bin (11,0)
Bin (11,1)
Bin (11,2)
Bin (11,3)
Bin (10,0)
Bin (10,1)
Bin (10,2)
Bin (10,3)
Bin (9,0)
Bin (9,1)
Bin (9,2)
Bin (9,3)
Bin (8,0)
Bin (8,1)
Bin (8,2)
Bin (8,3)
Bin (7,0)
Bin (7,1)
Bin (7,2)
Bin (7,3)
Bin (6,0)
Bin (6,1)
Bin (6,2)
Bin (6,3)
Bin (5,0)
Bin (5,1)
Bin (5,2)
Bin (5,3)
1e−6
1.5
1.0
0.5
0.0
−0.5
−1.0

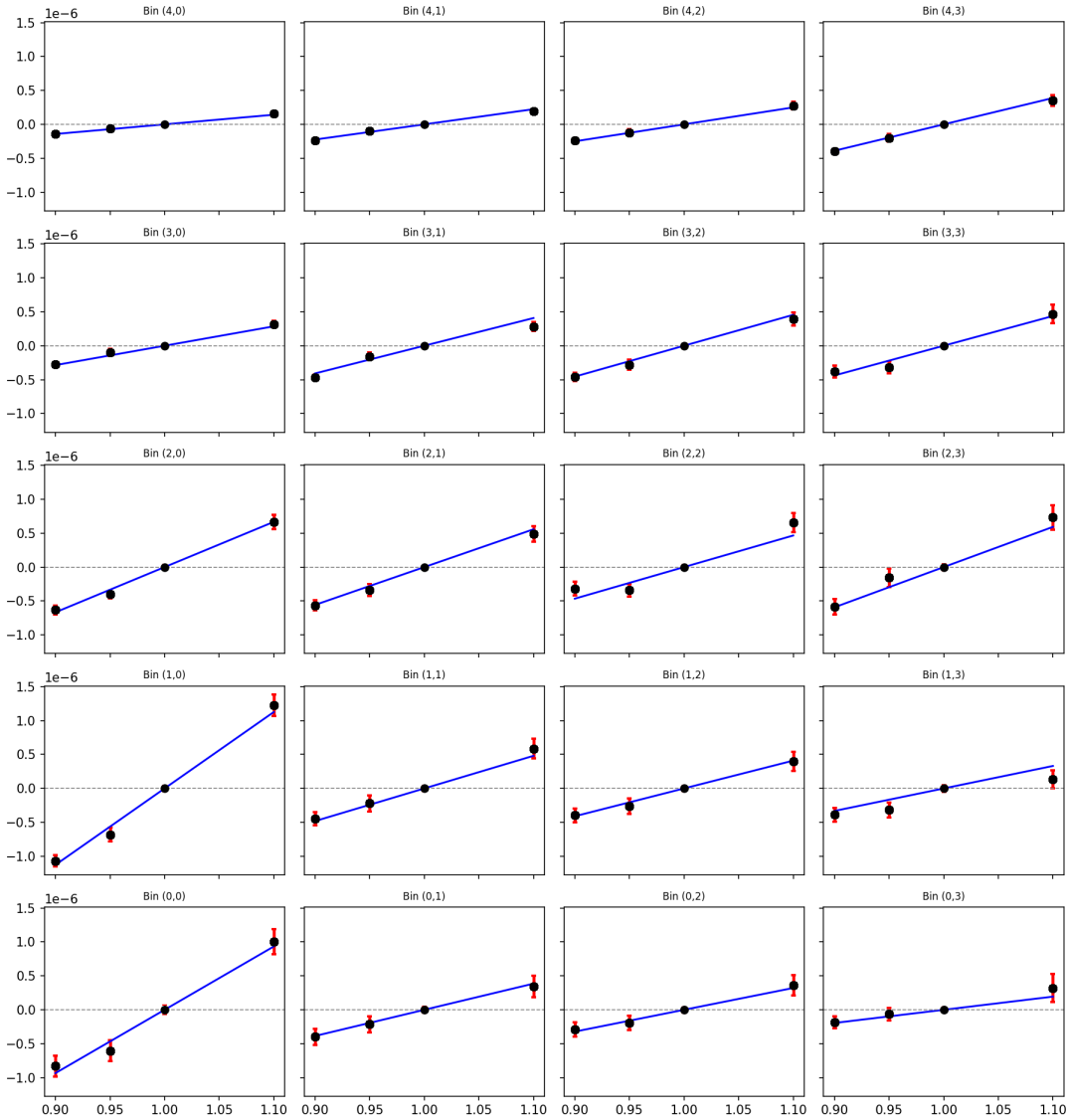

Figure A.2: Fits of the varied absorption length of ARCA21 in every bin of the binning (Energy, zenith) = (12, 4). Bin (0, 0) refers to the bin with the lowest energy and smallest cos(zenith), whereas bin (11, 3) refers to the highest values on both binning axes. The event numbers per bin and second are plotted for each simulation of the varied absorption length (abs90, abs95, abs100, abs110), where the baseline MC simulation abs100 is subtracted. The linear fit (blue line) is forced to go through abs100 and accounts for uncertainties in the histogram (red error bars).

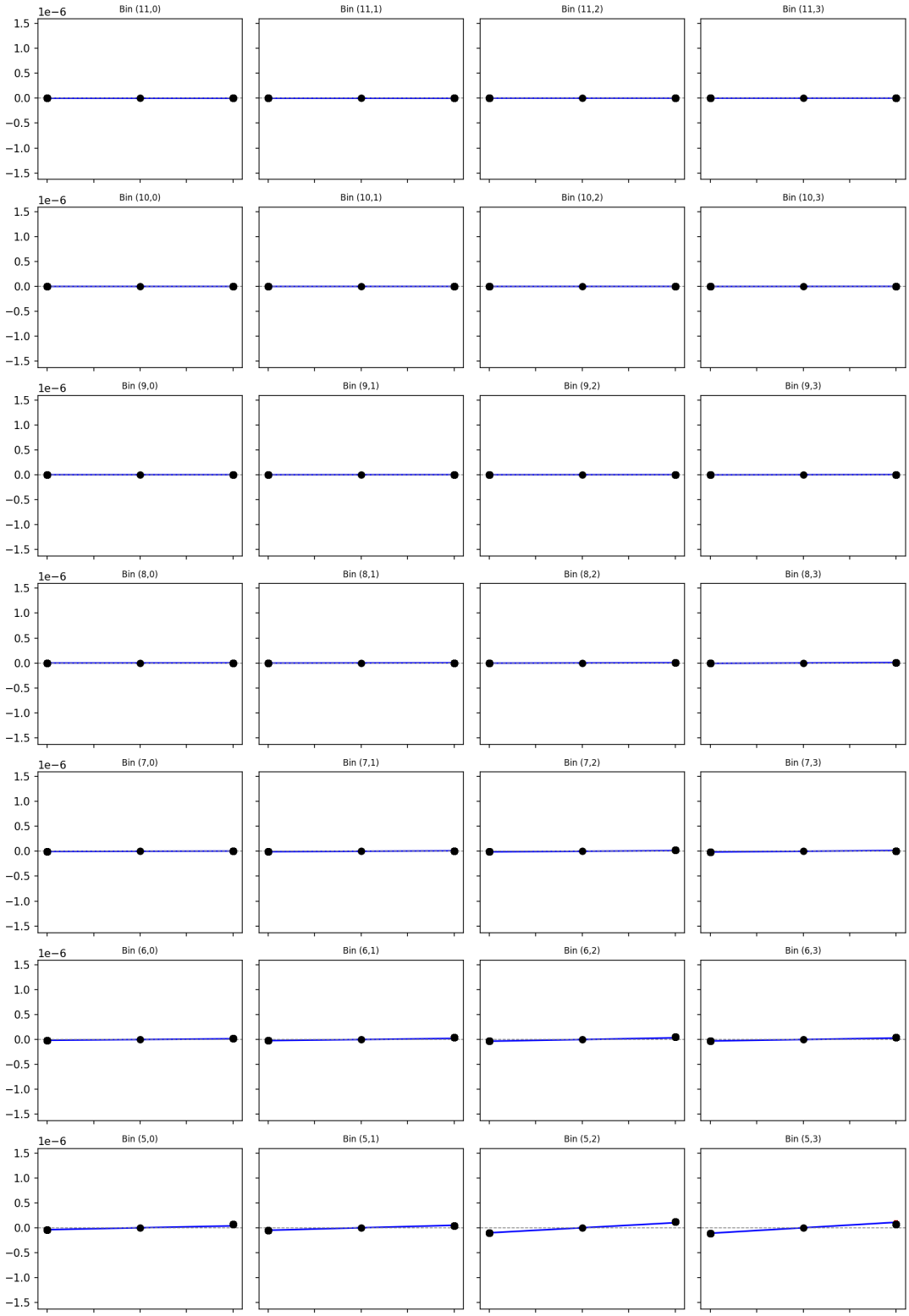
Bin (11,0)
Bin (11,1)
Bin (11,2)
Bin (11,3)
Bin (10,0)
Bin (10,1)
Bin (10,2)
Bin (10,3)
Bin (9,0)
Bin (9,1)
Bin (9,2)
Bin (9,3)
Bin (8,0)
Bin (8,1)
Bin (8,2)
Bin (8,3)
Bin (7,0)
Bin (7,1)
Bin (7,2)
Bin (7,3)
Bin (6,0)
Bin (6,1)
Bin (6,2)
Bin (6,3)
Bin (5,0)
Bin (5,1)
Bin (5,2)
Bin (5,3)
1e−6
1.5
1.0
0.5
0.0
−0.5
−1.0
−1.5

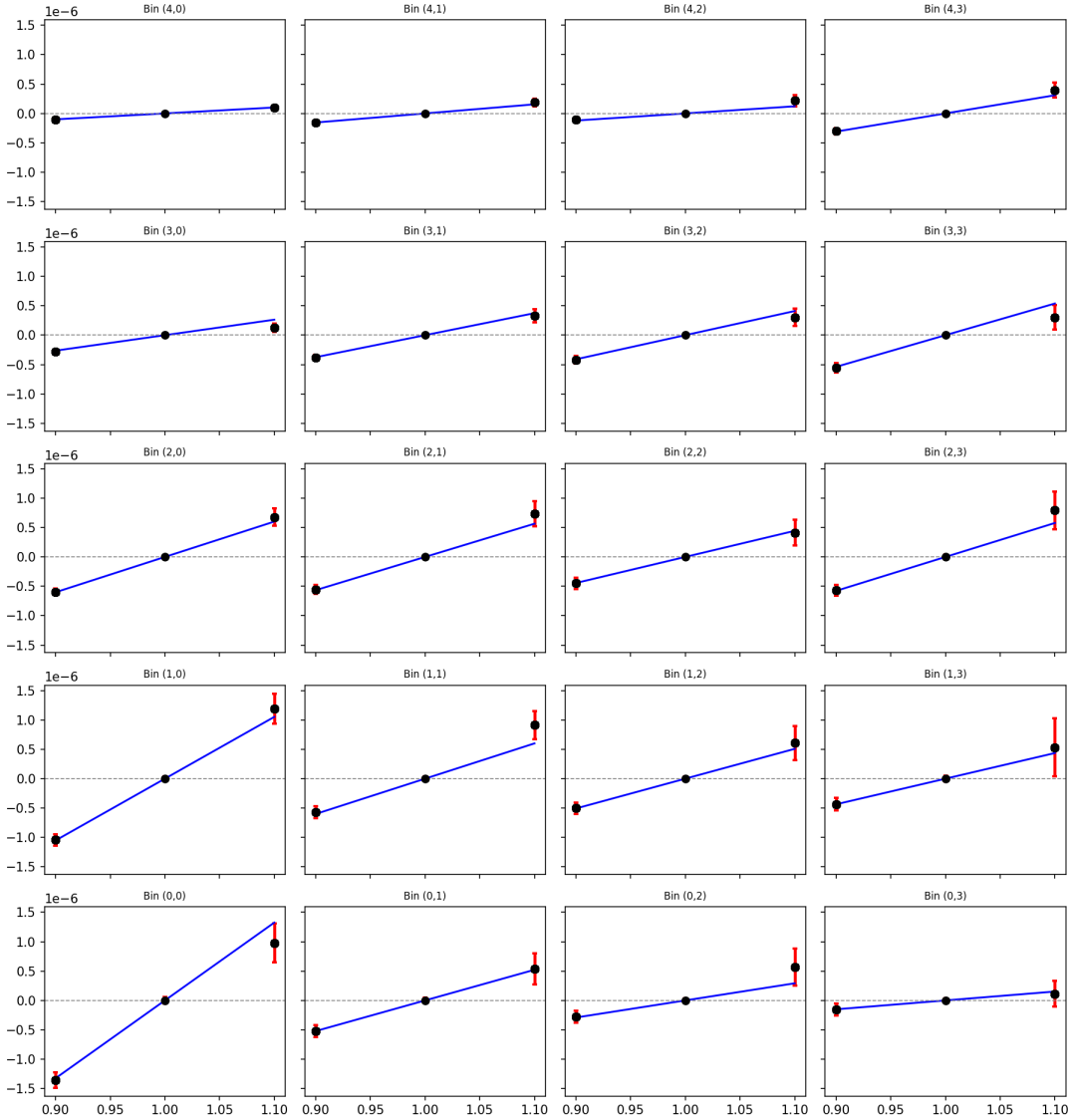

Figure A.3: Fits of the varied quantum efficiency of ARCA21 in every bin of the binning (Energy, zenith) = (12, 4). Bin (0, 0) refers to the bin with the lowest energy and smallest cos(zenith), whereas bin (11, 3) refers to the highest values on both binning axes. The event numbers per bin and second are plotted for each simulation of the varied quantum efficiency (QE90, QE100, QE110), where the baseline MC simulation QE100 is subtracted. The linear fit (blue line) is forced to go through QE100 and accounts for uncertainties in the histogram (red error bars).

B Appendix - Gingerbread Tasting

In Germany, especially before Christmas, people often ask which type of gingerbread they should buy. Gingerbread is a very popular baked good at Christmas time in Germany. The tradition of baking honey-sweetened bread dates back several hundred years [ii]. In principle, it was made all across the country. However, local variations emerged. In Aachen, the Aachener Printen became popular in the 19th century. Meanwhile, in Nuremberg, special gingerbread bakeries were mentioned in the history books as early as the 14th century [iii]. The question of which version is the best remains, however.
Therefore, the people at ECAP tasted in the season 2024 different versions of Aachener Printen and Nürnberger Elisenlebkuchen. After trying a piece of each type of gingerbread, they could rate it in four categories: taste, texture, optical appearance, and how Christmassy it made them feel. In each category, the scoring was from one to five Christmas trees. The descriptions for the scores were: one Christmas tree means poor, two means bad, three means OK, four means good, and five means great. The Aachener Printen that were tested were traditional hard Printen, soft Printen and dessert Printen. The gingerbread tested was all Nürnberger Elisenlebkuchen from different bakeries: Düll, Beck, Woitinek, Witte and Aldi. The tasting was not a blind study, all participants knew which type of gingerbread they were tasting, and the number of participants varied between 11 and 15 for the different types of gingerbread. This also does not match the objectives of a representative study, it only shows the preferences of the people who participated in the tasting.
The gingerbread tasting results are shown in Figure B.1. The different gingerbreads are listed on the y-axis, where the coloured lines indicate the mean values of the rating results in each category. The color-shaded areas indicate the uncertainties on that. To also reflect on an overall result, the black line shows the mean values of the different category ratings for each gingerbread. The colored squares show the best and worst-rated gingerbread in every category.
On this basis, the Christmassy feeling and the dessert's appearance do not have to correlate: the Printen dessert has the worst Christmassy feeling, but the best appearance. Aldi's gingerbread had the worst overall result, with the lowest score in three categories. It is the only gingerbread baked in an industrial bakery. All the others are from smaller, local bakeries. Woitinek's gingerbread won in three categories and

[ii] from https://de.wikipedia.org/wiki/Aachener_Printen
[iii] from https://de.wikipedia.org/wiki/N%3%Brnberger_Lebkuchen

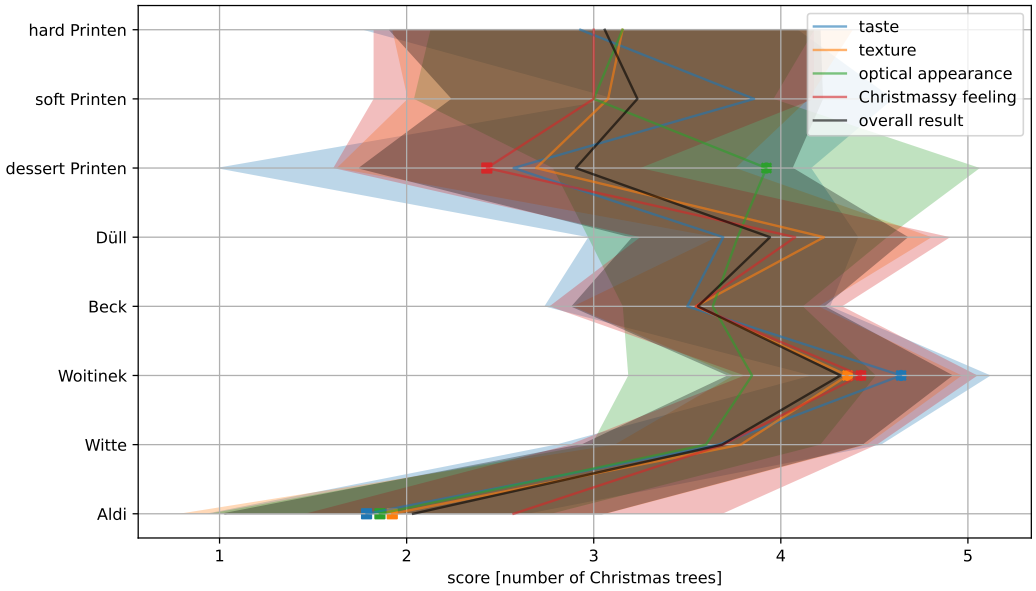

Figure B.1: This plot shows the results of the 2024 non-representative gingerbread survey at ECAP. The different gingerbreads listed on the y-axis were scored in units of Christmas trees by 11 to 15 participants on four categories: taste, texture, optical appearance, and Christmassy feeling. The colored lines indicate the mean value of the tasting result for each category, and the coloured areas the uncertainties. The overall result in black shows the mean of the ratings in the different categories.

therefore had the best overall result. In general, Printen have fewer Christmas trees in their overall results than gingerbread from small bakeries. However, a much larger variance of the Printen score is observed in comparison to that of the gingerbread. This may be because the testers are more familiar with the local gingerbread than the Printen. To investigate this further, it would be interesting to ask the participants where they are from.
Additionally, it would be interesting to see if the quality of the gingerbread changes over time. A survey is therefore planned for the next gingerbread season. With more participants, a better statistical result can also be obtained.
However, this should not stop you from just tasting all variants of gingerbread on your own - there are even more variants to try! Build your own opinion, and enjoy!

Acknowledgements

I would like to thank everyone who made last year so great. First of all, I would like to thank my supervisors. Oliver, thank you for answering all my questions (I had quite a lot) and for always helping me to improve my work! I would also like to thank Claudio for always offering advice when needed and for giving me the great opportunity to join the Collaboration meetings. I learned a lot from that experience.
I would also like to thank my wonderful colleagues from the Erlangen Tea Party (ETAP) office. You always made time to have tea with me or listen to my thesis problems. Thanks also to the coffee break group for the sometimes extensive breaks and great chats. And especially all people participating in the gingerbread survey!
Finally, I would like to thank everyone who proofread this thesis — you helped me a lot!

Declaration of Originality

I hereby confirm that I wrote this thesis by myself. Artificial intelligence in the form of DeepL, Grammarly, and ChatGPT was used in the following way:

- AI was used to improve the style and readability of this thesis. This includes corrections of grammar and spelling. AI was not used to generate full text passages or change the content of the text.
- AI was used to improve and verify the functionality of some code that was written in the scope of this thesis. Code snippets that were generated by AI were reviewed carefully before usage.

I confirm that I only used the indicated sources and tools.

Erlangen, 16.12.2025 **Anke Mosbrugger**